Investigating Device Physics in Bulk-Heterojunction Organic Solar Cells through Materials Engineering of Interfaces

Kevin M. O'Malley

A dissertation submitted in partial fulfillment of the requirements for the degree of

Doctor of Philosophy

University of Washington

2013

Reading Committee:

Alex K.-Y. Jen, Chair

David S. Ginger

D. Michael Heinekey

Program Authorized to Offer Degree:

Chemistry

©Copyright 2013
Kevin M. O'Malley

University of Washington

Abstract

Investigating Device Physics in Bulk-Heterojunction Organic Solar Cells through Materials Engineering of Interfaces

Kevin M. O'Malley

Chair of Supervisory Committee:
Professor Alex K.-Y. Jen
Department of Chemistry

We have designed and implemented several organic photovoltaic materials with the goal of engineering interfaces within bulk-heterojunction organic solar cells. In one project, we synthesized a C_{60} bis-adduct surfactant for use as a buffer layer between the photoactive layer and the thermally evaporated metal top contact of conventional structure, bulk-heterojunction organic solar cells. By systematically varying the work function of the contact metal, with and without the surfactant buffer layer, we gained insight into the physics governing the photoactive layer/metal interface and vastly improved the device performance. By applying Mott-Schottky analysis to the capacitance-voltage data obtained for these devices we were able to conclude that the surfactant modifies the metal work function to an appreciable extent, and allows for efficient charge extraction and significantly enhanced open-circuit voltage regardless of the chosen contact metal. This enhancement allowed us to use more air-stable metals that would ordinarily be prohibited due to suboptimal energy level alignment at the electron-collecting electrode. In a second line of investigation, we used impedance spectroscopy to probe the charge carrier recombination dynamics and their effects on device performance in organic solar cells composed of poly(indacenodithiophene-*co*-phananthrene-quinoxaline), as well as its fluorinated derivatives, and various fullerenes. We find that the morphology of the blended photoactive

layer has a strong influence on the electronic density-of-states distribution, which in turn directly affects the recombination rate as well as the achievable open-circuit voltage. We show that attempting to increase the open-circuit voltage through structurally tuning the energy levels of polymer and fullerene inadvertently introduces different bulk phase separation that leads to a reduction in photocurrent. We observe that the recombination lifetime decreases more dramatically with increasing excess photogenerated charge carrier density for blends with more finely separated phases and propose that the resulting increase in recombination surface area leads directly to reduced overall device performance, despite a marked increase in open-circuit voltage.

TABLE OF CONTENTS

LIST OF FIGURES

LIST OF TABLES

PREFACE

Portions of Chapter 2 were previously published as "Enhanced Open-Circuit Voltage in High Performance Polymer/Fullerene BHJ Solar Cells by Cathode Modification with a C_{60} Surfactant," K. M. O'Malley, C.-Z. Li, H.-L. Yip, A. K.-Y. Jen, *Adv. Energy Mater.* 2012, 2, 82, and have been reproduced with permission from the publisher. Copyright 2012 Wiley-VCH Verlag GmbH & Co. KGaA, Weinheim.

A manuscript based on the work presented in Chapter 3 of this dissertation was in preparation at the time of submission. A delayed publication of the dissertation was requested in order to maintain the ethical standards of published scholarly work, and it is expected that the manuscript and dissertation will be published concurrently.

ACKNOWLEDGEMENTS

I would first like to acknowledge my family for their support over the years. Graduate school can be a very isolating experience, and it has meant a great deal to me to have them so close. Their advice in times of difficulty has been most welcome, and I knew any one of them was never more than a phone call away. To my siblings Ryan and Erin, and my parents Bonnie and Neil, I offer my sincerest thanks.

I would like to thank my advisor, Alex Jen, for giving me the opportunity to undertake graduate research in his group. When I first began working with Alex, I knew absolutely nothing about the field of organic electronics, and was actually working on a project related to my undergraduate research in two-photon absorption microfabrication. After awhile, we both knew it would be a difficult road with only one person in the entire group that knew anything about this technique, and I began work on device engineering of organic solar cells. When I expressed a desire to know more about what made these photovoltaic devices tick, and specifically that I was interested in studying them more in-depth with a variety of spectroscopic techniques, Alex was very supportive. Working with Alex over the years has instilled in me a deep appreciation for independent research and what it takes to achieve scientific goals. I also owe a great debt to those Jen group members who have taken the time to teach me along the way: Steven Hau for teaching me not only how to reproducibly fabricate solar cells, but also how to navigate the often difficult path of graduate school, Kung-Shih Chen, Jingyu Zou, Chu-Chen Chueh and Nam-Chul Cho for their helpful conversation and in-lab camaraderie, Chang-Zhi Li for helping me understand the finer points of structure/property relationships in organic solar materials, and Angus Yip for keeping the organic photovoltaics group pointed in the right direction. I would also like to thank Cody Schlenker for always taking time out of a very busy schedule to give me a different perspective on the challenges I faced with my own work. In addition to being an accomplished scientist, Cody is very approachable and is both passionate about his work and helping others achieve success in their own research.

Finally, I would be remiss not to acknowledge the friends I have had the great pleasure of knowing since moving to Seattle. Our starting class of graduate students became unusually close very quickly, and remains so even now that most of us have moved on. I would especially like to thank Sam Berweger and Brad MacLeod for the good times we shared, and for always reminding me that there is such a thing as life outside of the lab.

DEDICATION

To my mother, Bonnie: You have my deepest respect and admiration. Thank you for your unwavering support in everything I have ever undertaken, and for teaching me the true meaning of perseverance.

CHAPTER 1:
Organic solar cells

1.1 Introduction

Organic solar cells (OSC) represent a unique alternative renewable energy source combining the potential benefits of comparatively low-cost fabrication, solution processing and wide application through the versatility afforded by appropriate device design.[1] The advantages demonstrated by OSC over their inorganic counterparts have generated extensive research efforts over the past fifteen years and significant contributions to the field have increased our basic knowledge of organic electronics and carried the concept of OSC in particular one step closer to market viability. The key advantage with OSC is the potential for high throughput fabrication based on solution processing, which could be incorporated into pre-existing roll-to-roll printing infrastructures,[2] leading to a lower cost of production and ultimately a lower cost per watt ratio. This facility of fabrication immediately opens avenues for innovative device applications usually prohibited in traditional solar cell technology such as the ability to process the cell on flexible substrates or to integrate modules into semi-transparent, power generating windows. Ultimately, it is the scalability and lower production cost of OSC that will be attractive in the energy market.

The advances in OSC technology have indeed been rapid, leading to an impressive body of scientific literature detailing significant improvements in device performance, with photovoltaic power conversion efficiencies reaching on average above 7% and ~10% in state-of-the-art devices,[3,4] through a combination of materials design, interface engineering and understanding of basic device physics. Although the outlook for OSC is certainly bright, there remain a number of significant advances to be made and a large parameter space to be optimized.

Specifically, OSC currently suffer from an increased number of potential degradation pathways over their inorganic counterparts, leading to reduced temporal stability and usable lifetime. Other drawbacks include currently lower efficiencies than more mature solar technologies such as silicon, an enhanced sensitivity to ambient operating conditions such as heat, oxygen and moisture and an as yet poorly understood dependence of performance on active layer morphology. All of these problems are likely soluble within the framework of the multidisciplinary approach being taken, and the goal of stable, reasonably efficient and cost-effective devices is rapidly approaching reality. This work focuses on improving device performance through materials engineering and probing the physics of interfaces in operating OSC, with the goal of rational design of future energy converting materials and device architectures.

1.2 Development of modern organic solar cells

1.2.1 The planar heterojunction organic solar cell

The purpose here is to contextualize the work contained in this dissertation in terms of the evolving complexity of interfaces in OSC. Not long after the first report of conducting polymers in 1977,[5] extensive research efforts were launched with the aim of synthesizing new classes of conjugated organic materials for use in traditional semiconductor electronic devices. Although the first bilayer OSC was reported by Tang in 1986,[6] the photoactive materials were thermally evaporated small molecules, and the first instance of photo-excited charge transfer from a conjugated polymer to a fullerene, representative of the most common OSC today, was actually demonstrated by Sariciftci et al. in 1992.[7] This heterojunction architecture showed a large improvement over its single component predecessors by virtue of a significant energy

offset between the highest occupied molecular orbital (HOMO) of the electron donating polymer and lowest unoccupied molecular orbital (LUMO) of the accepting fullerene. This energy offset provided a thermodynamic driving force for separating the coulombically bound electron-hole pair, known as an exciton, into free charge carriers which could then be transported to their respective electrodes under an asymmetric potential across the photoactive layer set up by the difference in electrode work functions. Despite much improved photovoltaic properties, planar heterojunction devices suffered from one major drawback. Exciton diffusion lengths were determined to be on the order of 10 nm,[8] which meant any excitons formed further from the heterojunction were very likely to be lost to recombination. This represented a photocurrent loss mechanism that could be partially mitigated by decreasing the absorber layer thickness, but at the obvious cost of optical density.

1.2.2 The bulk-heterojunction organic solar cell

In 1995, Yu et al. reported on the first OSC to utilize a bulk-heterojunction (BHJ) photoactive layer composed of a high volume density of polymer/fullerene interfaces.[9] The intimately mixed domains were found to be on the same scale as the exciton diffusion length, which meant the photoactive layer thickness was no longer so restricted; more photogenerated excitons could be formed, and most could now find an interface before recombination occurred, leading to significantly increased external quantum efficiencies. It is fair to say that the introduction of the BHJ OSC represents a paradigm shift in the field, and the majority of scholarly work since has been focused on further optimizing performance through materials and architecture engineering, while simultaneously attempting to gain better insight into the physics that govern such devices though a wide range of spectroscopic methods. New, low bandgap polymers make it possible to absorb more of the solar spectrum, creating the potential for greater

charge generation, while concurrent studies have shown the importance of certain processing conditions on these devices such as solvent choice, drying rates and photoactive layer annealing.[10–12] Control over the active layer morphology has proven very important for device performance, and it has been well characterized from a variety of angles,[13–15] however the mechanisms by which it determines device performance and stability are still debated in the community.

1.2.3 Inverted organic solar cells

In 2006 the concept of an inverted BHJ OSC was introduced,[16,17] which immediately attracted attention on account of improved temporal stability and compatibility with roll-to-roll processing. It is well known that low work function metals like Ca and Al, typically used to cap conventional structure OSC, are prone to oxidation leading to significantly decreased device lifetimes under ambient conditions.[18] In an inverted cell, the polarity of the device is reversed and holes are collected from the top electrode instead of electrons, which opens the door for the development and implementation of a variety of new electron and hole transporting materials at the charge-collecting interfaces. The inverted cell also paved the way for new, multi-junction OSC, wherein interface engineering becomes critical.[19] It is clear then, with the increasing complexity of device design, that there is a need to understand the physics of interfaces in OSC as well as the very practical need for new materials in order to increase device performance and longevity.

1.3 Thesis statement

We have designed and implemented several organic photovoltaic materials with the goal of engineering interfaces within BHJ OSC. In Chapter 2, the implementation of a C_{60} bis-adduct surfactant as a buffer between the photoactive layer and the thermally evaporated metal top contact of a conventional structure organic solar cell is described. By systematically varying the work function of the contact metal, with and without the surfactant buffer layer, we gained insight into the physics governing the photoactive layer/metal interface and vastly improved the device performance. By applying Mott-Schottky analysis to the capacitance-voltage data obtained for these devices we were able to conclude that the surfactant modifies the metal work function to an appreciable extent, and allows for efficient charge extraction and significantly enhanced open-circuit voltage regardless of the chosen contact metal. This aspect allowed us to use more air-stable metals that would ordinarily be prohibited due to suboptimal energy level alignment at the electron-collecting electrode.

In Chapter 3 we discuss the use of impedance spectroscopy to probe charge carrier recombination dynamics at the donor polymer/acceptor fullerene interface in devices composed of poly(indacenodithiophene-*co*-phananthrene-quinoxaline) (PhanQ), as well as its fluorinated derivatives, and various fullerenes. We find that the morphology of the blended photoactive layer has a strong influence on the electronic density-of-states (DOS) distribution, which in turn directly affects the recombination rate as well as the achievable open-circuit voltage. We show that attempting to increase the open-circuit voltage through structurally tuning the LUMO level of the fullerene inadvertently introduces different polymer/fullerene phase separation that leads to a reduction in photocurrent. We observe that the recombination lifetime drops off more steeply with increasing excess photogenerated charge density for blends with more finely

separated phases and propose that the resulting increase in recombination surface area leads directly to reduced overall device performance, despite a marked increase in open-circuit voltage. We close with a discussion of the implications of our findings for future materials design.

CHAPTER 2:
Engineering the photoactive layer/top electrode interface

2.1 General operating principles of organic solar cells

2.1.1 Photovoltaic energy conversion and current-voltage characteristics

Figure 2-1 schematically illustrates the basic operation of a typical polymer:fullerene BHJ solar cell. Photons are usually absorbed mostly by the polymer phase, whereupon the aforementioned excitons are generated. The excitons then diffuse to donor/acceptor interfaces and charge transfer of the electron to the fullerene phase occurs. Fully separated charges are then transported to the appropriate electrodes, holes through the polymer to the anode and electrons through the fullerene to the cathode, for collection and extraction to an external circuit where they can perform electrical work. The primary figure of merit for OSC is the power conversion efficiency (PCE), which is a ratio of the maximum power output of the solar cell to the input power of incident light.

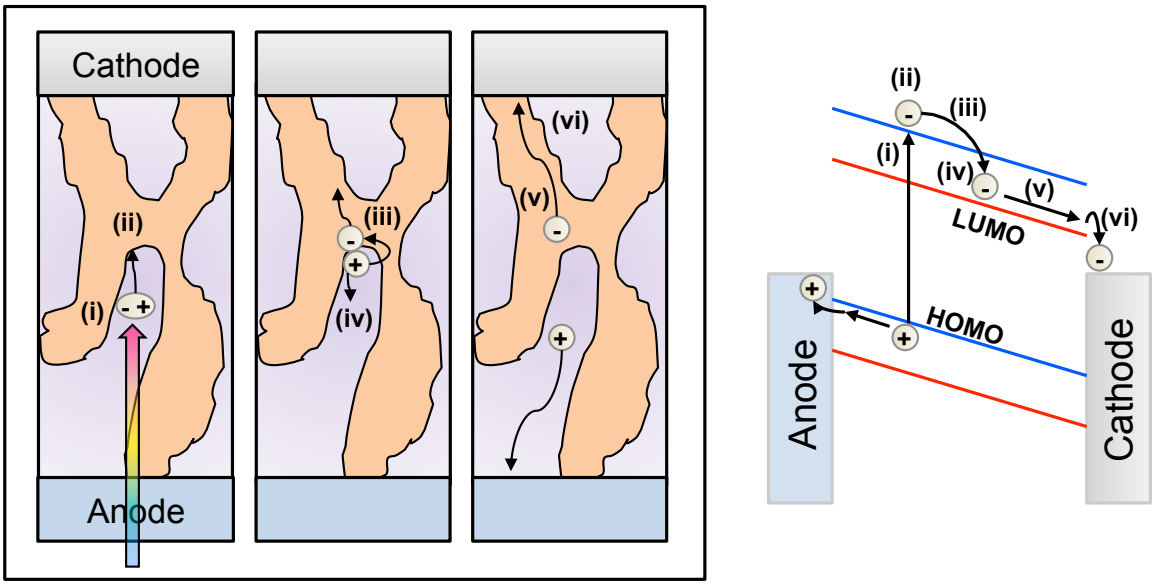

Figure 2-1: Mechanism of photovoltaic energy conversion in a conventional structure bulk-heterojunction organic solar cell. The individual steps are labeled on the (boxed, left) physical diagram and (right) simplified energy diagram. (i) exciton generation by photon absorption in the polymer phase. (ii) exciton diffusion to the polymer/fullerene interface. (iii) charge transfer of the electron to the fullerene. (iv) charges overcome coulombic attraction, separation of the exciton occurs. (v) charges are transported to respective electrodes. (vi) charge collection and extraction to external circuit.

The PCE is calculated from the short-circuit current (I_{SC}) (where applicable J will be used to denote current density, e.g. short-circuit current density is J_{SC}), open-circuit voltage (V_{OC}) and fill factor (FF) parameters extracted from I-V sweeps under standardized illumination conditions as:

$$(2\text{-}1) \qquad PCE = \frac{P_{max}}{P_{light}} = FF\left(\frac{I_{SC}V_{OC}}{P_{light}}\right)$$

Figure 2-2 shows typical J-V curves in the dark and under illumination for a solar cell based on a blend of PhanQ and [6,6]-phenyl-C_{71}-butyric acid methyl ester ($PC_{71}BM$). At high reverse bias, the current saturates to a value J_{sat} limited by the kinetics of charge collection at the electrodes and represents the maximum output current density of the device. Notably, J_{SC} is usually less than J_{sat} due to a variety of potential loss mechanisms including leakage current and lower shunt resistance within the bulk. As the bias voltage is increased, the device approaches the so-called flatband condition, wherein the voltage difference set up by the asymmetric electrode work functions is recovered and no photocurrent is observed. The product of J_{SC} and V_{OC} represents

the ideal, maximum power output of the OSC, whereas the actual maximum power output is usually much less. The FF relates these last two quantities and gives a qualitative measure of the ideality of the solar cell: the greater the FF, the more "square" the J-V curve and the closer the cell is to performing as an ideal photodiode.

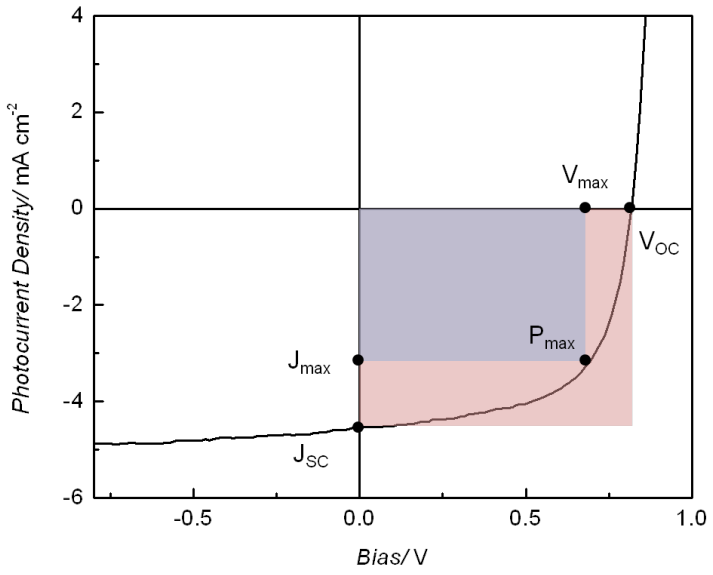

Figure 2-2: An example of a J-V curve for a bulk-heterojunction solar cell studied in this work.

2.1.2 The open-circuit voltage

The a large part of this dissertation focuses on understanding and improving V_{OC} in BHJ OSC, hence a more detailed description of the device parameter is given here. The terms HOMO and LUMO typically refer to the relevant molecular orbital energy levels on a single molecule. However, because the materials of interest in an OSC are only weakly interacting, these levels can be considered preserved in the disordered, extended solid of the BHJ, and the concept of band transport appropriate for traditional crystalline Si solar cells has only limited applicability.[20] Instead, this disorder has the effect of broadening the HOMO and LUMO from single levels into manifolds typically described by a Gaussian DOS. Under illumination these states become

populated by charge carriers, effectively splitting the electron and hole quasi-Fermi levels, and it is this potential energy difference between electrons and holes that sets the upper limit for achievable V_{OC} in a device. This last statement assumes the critical condition that the work functions of the electron and hole-collecting electrodes are properly aligned to the appropriate quasi-Fermi levels, which is to say Ohmic contact is formed at the charge-collecting interfaces. To this end, several approaches have been employed to modify the organic/electrode interface in order to maximize V_{OC}. In conventional structure BHJ OSC, the conducting polymer poly(ethylenedioxythiophene):poly(styrenesulfonate) (PEDOT:PSS), is used to modify the surface of the hole-collecting anode. With a work function (WF) closely matching the hole-transport level of a wide range of donor polymers, on the order of 5 eV below vacuum, PEDOT:PSS is capable of forming excellent electrical contact with the organic active layer of the device at the anode. Therefore, much attention has been paid to engineering the energy level alignment at the organic/cathode interface in efforts to improve device performance.[21,22]

2.2 Implementation of a C_{60} bis-adduct surfactant buffer layer

Previously, we reported a new bis-adduct fullerene surfactant (C_{60}-bis) that functions as an efficient electron selective material when inserted between various BHJ layers and an Al cathode, which led to improved performance in organic photovoltaic devices.[23] In order to better understand the origin of efficiency enhancement when C_{60}-bis is incorporated into OSC, we have studied the electronic properties at the BHJ/C_{60}-bis/metal interface. We have performed the study based on the high performance PhanQ:$PC_{71}BM$[24] BHJ system and have investigated the effect of different cathode metals (Al, Ag, Cu) on the PCE and stability of the OSC devices. Since the C_{60}-bis is processed from a methanol solution, there is no degradation of the underlying

PhanQ:$PC_{71}BM$ active layer. This device architecture effectively achieves a desirable phase-segregation wherein no polymer is in contact with the electron-collecting electrode, resulting in superior charge selectivity at the metal/active layer interface.

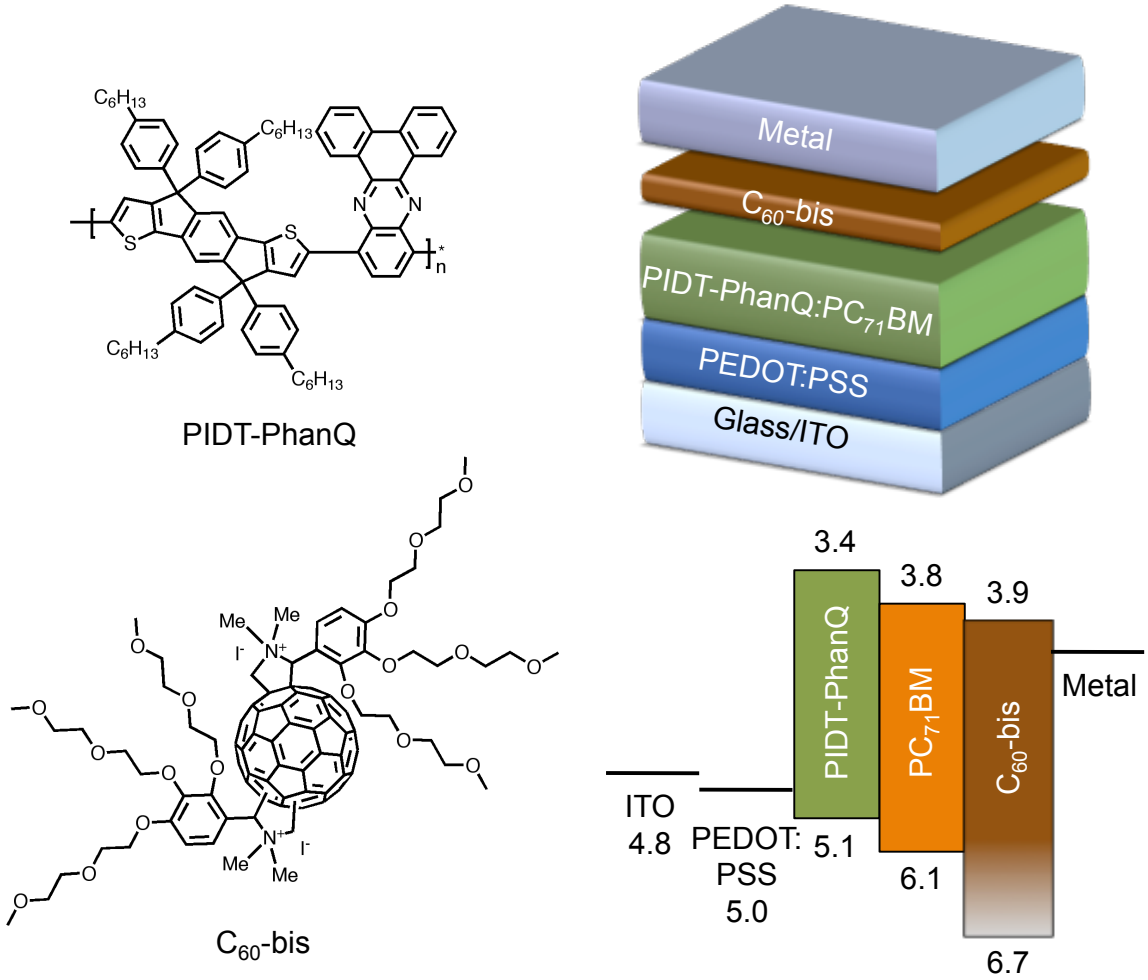

Figure 2-3: Chemical structures of (top, left) PhanQ and (bottom, right) C_{60}-bis surfactant; and the (top, right) conventional structure OSC architecture with (bottom, right) corresponding energy level diagram.

Figure 2-3 shows the energy level diagram for the completed device, the device architecture and chemical structures of the polymer and surfactant. The HOMO level of the surfactant is sufficiently deeper than that of the polymer, effectively blocking holes generated in the photoactive layer from reaching the cathode and potentially recombining with electrons before they can be collected, which is evidenced by an increase in J_{SC}.

As has already been mentioned, it is desirable to select an electron-collecting electrode with a lower work function close to the electron quasi-Fermi level. However, in so doing, the contact becomes susceptible to rapid oxidation under ambient conditions. To circumvent this issue, we have fabricated devices with higher WF metals less prone to oxidation, which are shown to perform better than Al devices over time. Remarkably, the V_{OC} appears to be independent of the choice of cathode metal when C_{60}-bis is used as a buffer layer.

2.3 Experimental details

ITO-coated glass substrates (15 Ω sq^{-1}) were cleaned sequentially by sonication in detergent and deionized water, acetone and isopropanol. After drying under a N_2 stream, substrates were air-plasma treated for 30 s. A ca. 35 nm layer of PEDOT:PSS (Baytron® P VP Al 4083, filtered through a 0.45 μm nylon filter) was spin-coated onto the clean substrates at 5 kRPM and annealed at 140˚C for 10 min. The substrates were transferred to a N_2-filled glovebox where a homogeneously blended solution of PhanQ:$PC_{71}BM$ (40 mg/ml in o-dichlorobenzene stirred overnight in glovebox, 1:3 polymer:fullerene by weight) was spin-coated at 2 kRPM, producing an active layer ca. 100 nm thick, and annealed at 110˚C for 10 min. Substrates requiring a layer of fullerene surfactant were briefly transferred out of the glovebox (total ambient exposure <10 min) and a ca. 2-5 nm thick film of C_{60}-bis surfactant (1 mg/ml in methanol) was spin-coated at 5 kRPM. The substrates were then transferred back into the glovebox and annealed at 110˚C for 5 min to drive off any remaining solvent prior to metal deposition. Metal electrodes were deposited at a base pressure $<1x10^{-6}$ Torr through a shadow mask, defining an active device area of 4.64 mm^2. Ag and Cu were deposited at a rate of 1 Å s^{-1} and Al was deposited at a rate of 4 Å s^{-1}.

For devices to be characterized by XPS, ITO-coated glass substrates were prepared as above sans air-plasma treatment. Al, Ag and Cu were deposited over the entire substrate surface at a rate of 1 Å s^{-1}. Substrates requiring a thin layer of fullerene surfactant were transferred out of the glovebox and a solution of C_{60}-bis surfactant was spin-coated from methanol using the same conditions as above. After transfer back into the glovebox, all substrates were heated at 70˚C for 5 min to evaporate any remaining methanol prior to being sealed with parafilm in 20 ml glass vials under N_2 for transport to the XPS laboratory.

J-V characteristics of the unencapsulated devices were measured in ambient conditions using a Keithley 2400 source meter under AM 1.5 G (100 mW cm^{-2}) irradiation simulated by an Oriel xenon lamp (450 W). AM 1.5 G illumination was confirmed by means of calibration to a standard silicon photodiode (Hammamatsu) which can be traced to the National Renewable Energy Laboratory. External quantum efficiency spectra were obtained by measuring the photocurrent response of the device using chopped, monochromated light from the same xenon lamp in conjunction with a Stanford Research Systems SR830 lock-in amplifier under ambient conditions. Mott-Schottky analysis was performed in a N_2-filled glovebox in the dark using a Signatone probe station interfaced with a Hewlett-Packard HP4284A LCR meter. The 1 kHz AC field applied during measurement was kept at an amplitude of 20 mV to maintain response linearity. Capacitance-voltage characteristics measured thusly were obtained using devices prepared as above with an active area of 10.08 mm^2. Work function determination via XPS is described in detail in the Appendix. Briefly, the secondary electron cutoff (SEC) spectrum of each sample was measured under ultra-high vacuum ($<5x10^{-9}$ Torr) using a PHI 5000 VersaProbe (Ulvac-Phi, Inc.) employing a focused, monochromated Al K-α x-ray source and a hemispherical analyzer. Proper referencing of the SEC edge to that of Ar^+ ion sputter-cleaned,

polycrystalline gold allowed for accurate determination of the sample work functions with a reproducibility of about 0.05 eV.

2.4 Results and discussion

Figure 2-4 shows the J-V characteristics for devices fabricated with different cathode metals both with and without a C_{60}-bis buffer layer. The V_{OC} for devices with an Al cathode is consistently lower than that of Cu and Ag devices, which can be attributed to the rapid oxidation of Al in air. The non-ideal nature of this interface also manifests in a modest fill factor (FF) of 0.51 and an overall PCE of 3.22%. In contrast, when a layer of C_{60}-bis is used, the PCE increases to 5.87% as a result of an increase in J_{SC}, FF and most notably V_{OC}. In addition, the shunt resistance (R_{SH}) is shown to increase for all metals in the case of C_{60}-bis, which provides evidence of lower leakage current under illumination. Performance data for all devices are summarized in Table 2-1.

To investigate the improvement in J_{SC}, external quantum efficiency (EQE) spectra (Figure 2-4) were obtained for Al, Ag and Cu devices. The spectra exhibit an almost constant increase across the entire wavelength range for each case when the surfactant layer was inserted. This indicates the improvement in J_{SC} is due entirely to the inclusion of the surfactant and a concurrent decrease in recombination resistance at the organic/electrode interface, rather than a change in bulk morphology.

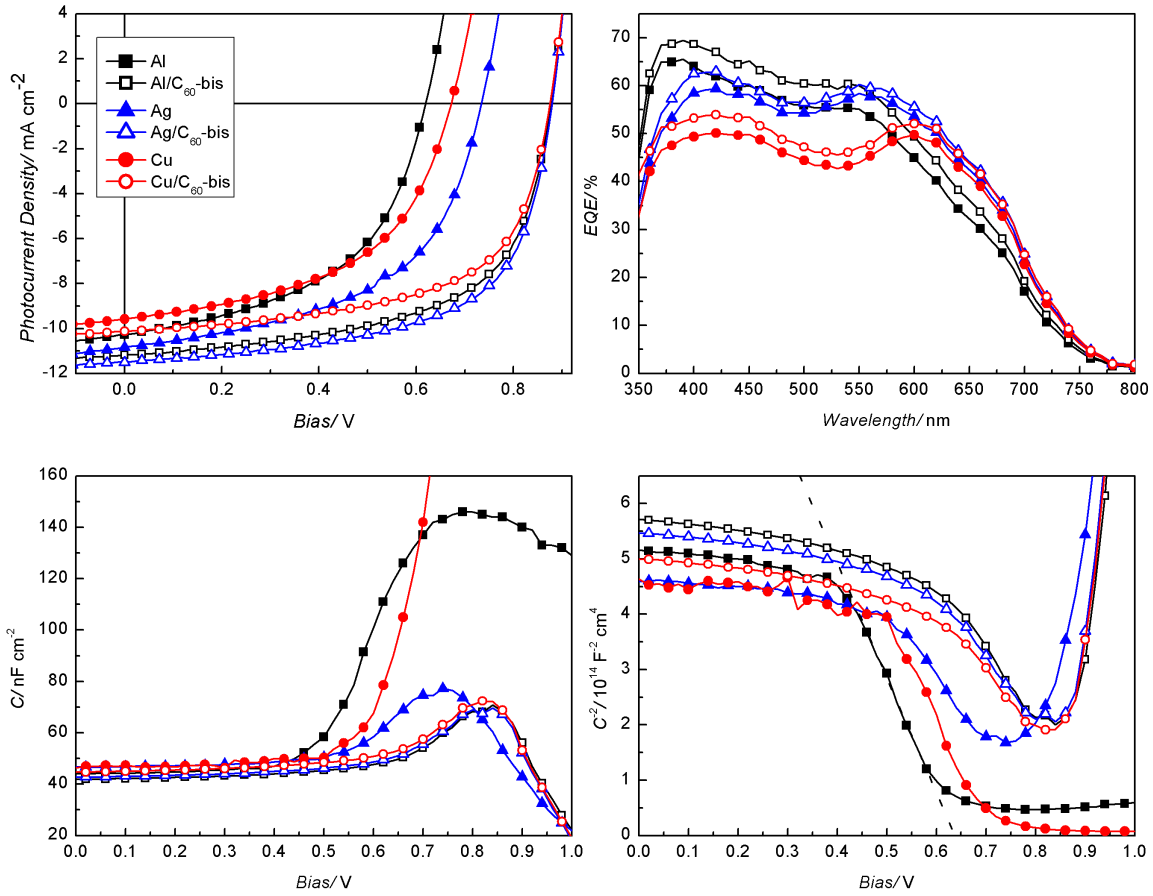

Figure 2-4: Performance data for PhanQ devices fabricated with different choice of cathode metal, with and without C_{60}-bis interlayer. (top, left) J-V curves and (top, right) EQE spectra show increases in V_{OC} and J_{SC}, respectively. (bottom, left) Capacitance-voltage and (bottom, right) Mott-Schottky analysis explain increased V_{OC} in terms of the built-in potential of the Schottky depletion region at the cathode. The dashed line is a linear fit to the data for V_{BI} extraction.

To further demonstrate the utility of C_{60}-bis as an interfacial layer, the PCE of devices with different cathode metals were tracked over a period of time under exposure to ambient conditions. Figure 2-5 shows the normalized PCE for unencapsulated devices with and without C_{60}-bis over 100 h in air. As expected the performance of Al devices drops off rapidly, even with the inclusion of the fullerene surfactant, which is likely due to the uptake of oxygen and water molecules and their subsequent diffusion to the metal/organic interface. The Ag and Cu devices remain very stable, however, with the Cu/C_{60}-bis retaining nearly 90% of its original PCE after the entire period of ambient exposure.

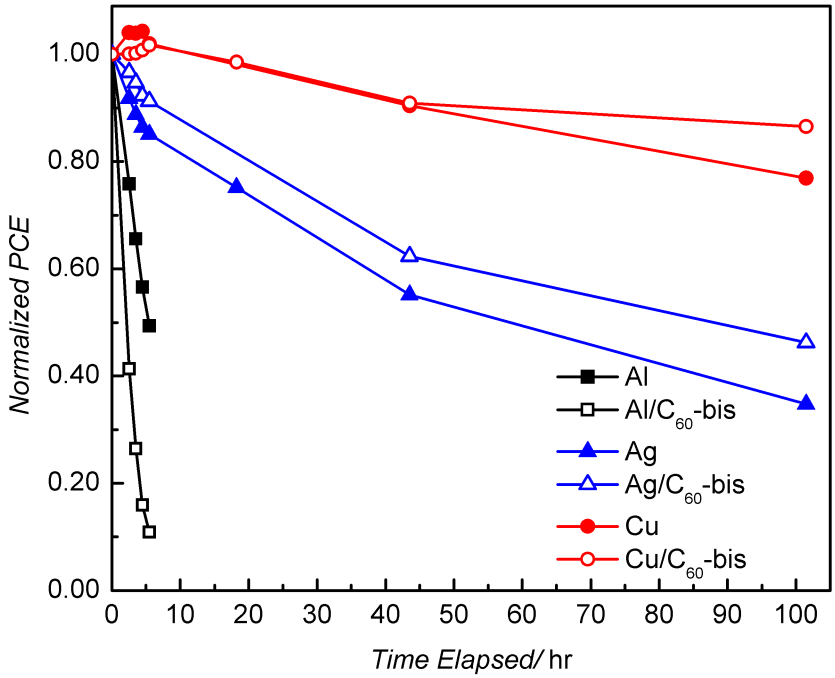

Figure 2-5: Normalized PCE for Al, Ag and Cu devices with and without C_{60}-bis under ambient conditions.

By far the most obvious benefit of C_{60}-bis is a strongly enhanced V_{OC}. To further investigate the dramatic increase in V_{OC} when C_{60}-bis is used, capacitance-voltage characteristics (C-V) were obtained and devices were analyzed via Mott-Schottky (MS) analysis. It has previously been shown that, due to the intrinsic p-doped nature of semiconducting polymers, a Schottky contact is formed upon deposition of the cathode onto the photoactive layer.[25] The depletion zone formed at this interface is modulated by the applied voltage under reverse and low (<1.5V) forward bias. Boix *et al*. showed that band-bending results in the vicinity of the cathode, allowing extraction of the built-in potential (V_{BI}) and impurity concentration (N) of the region by application of $C^{-2} = (2/q\varepsilon N)(V_{BI} - V)$ to the appropriate bias voltage range.[26] It should be stressed here that V_{BI} relates only to the depletion region, and not to the built-in field of the entire device.

Figure 2-4 shows the capacitance behavior of all devices as a function of bias voltage. The low capacitance region up to about 0.5 V has been attributed to the capacitance of the depletion layer, whereas a further increase in forward bias voltage yields a peak in the capacitance related to the storage of minority carriers in the bulk.[25] Also shown in Figure 2-4 are the MS plots for all

devices. At moderate to high reverse bias, C^{-2} tends to reach a steady value related to the geometric capacitance of the organic material, which has become fully depleted of majority carriers and can be viewed as a classical dielectric. As previously mentioned, the linear region under low forward bias is related to the formation of a Schottky contact and can be fitted to a plot of C^{-2} versus bias voltage. Extrapolation of the linear fit line to the intercept on the bias axis directly yields V_{BI} for the device. Once a value for V_{BI} has been obtained, an impurity concentration N and depletion width $w = (2\varepsilon V_{BI}/qN)^{1/2}$ corresponding to zero applied bias can be extracted.[26,27] A dielectric permittivity of 3 has been assumed for calculations involving these equations.[27] MS analysis data, along with the relative shifts in V_{OC} and V_{BI}, are summarized in Table 2-2. Interestingly, the depletion width extracted from the capacitance-voltage data extends over almost the entire thickness of the active layer. When taken with the N values obtained from the same data, this indicates a consistent doping profile across the entire layer that changes negligibly by inclusion of C_{60}-bis. Since the change in the Fermi level of the active layer (E_{Fp}) can be approximated by $\Delta E_{Fp} = k_b T \ln(N_c/N_a)$,[27] where N_c and N_a are the dopant concentrations of the device with and without C_{60}-bis, respectively, it is reasonable to conclude that E_{Fp} does not change more than ca. 10 meV. When a semiconductor is placed in intimate contact with a metal, their respective E_F come into equilibrium by electrons being transferred "downhill" in energy.[20,28,29] If we reference V_{BI} to E_{Fp} by $V_{BI} = (E_{Fp} - \Phi_{cathode})$, where $\Phi_{cathode}$ is the cathode WF, then the difference in V_{BI} with and without C_{60}-bis can be attributed to a modification of $\Phi_{cathode}$ by the surfactant. Furthermore, since the relative shifts in V_{BI} closely follow those of V_{OC} for all three metals we can conclude that the observed increase in V_{OC} upon inclusion of C_{60}-bis is due to a dipole-induced shift in $\Phi_{cathode}$ at the interface.

To further investigate the energetics at the interface, WFs were obtained for Al, Ag and Cu with and without C_{60}-bis spin-coated on top and are summarized in Table 2-2. WFs of *in-situ*, sputter-cleaned Al, Ag and Cu films were measured to be 4.25 eV, 4.57 eV and 4.70 eV, respectively (Figure A2). Interestingly, the WFs of Ag and Cu with C_{60}-bis yield nearly the same value. Since sampling of the substrate at normal emission is highly surface sensitive, it is reasonable to assume these WF values correspond to the C_{60}-bis. As the material is taken to be an n-type semiconductor, one would expect E_F to be closer to the LUMO level than mid-gap, which matches well with our findings. It should be noted that the WFs of the organic overlayer may be subject to any band bending occurring at the metal/organic interface as a result of E_F equilibration. Additionally, it is likely that an unavoidable thin oxide layer formed on the Al sample when it was removed from the glovebox for C_{60}-bis deposition, as evidenced by a comparison of O1s peak intensity in XPS survey spectra for bare Al before and after sputter-cleaning with Ar^+ ions (not shown). These considerations might explain the lower WF of the modified Al cathode as compared to Ag and Cu.

It should be stressed that these conditions do not prevail for regular device fabrication since the cathode is deposited under high vacuum after spin-coating the C_{60}-bis layer outside the glovebox. Regardless, at a distance sufficiently far into the bulk of the photoactive layer only the effective WF of the C_{60}-bis modified cathode can be "seen" by the rest of the device. This ensures a constant difference between E_F^p and $\Phi_{cathode}$, and explains why V_{BI}, and consequently V_{OC}, is nearly the same for all three metals when C_{60}-bis is employed.

In conclusion, a C_{60} bis-adduct surfactant was used to modify the energy level alignment at the organic/cathode interface in conventional structure, BHJ OSC devices. A well-defined interface between the photoactive layer and the surfactant was ensured by virtue of process

solvent orthogonality. The large increase in device V_{OC} is independent of the choice of cathode metal due to pinning of the metal E_F to that of the C_{60}-bis upon equilibration. Mott-Schottky analysis of the interface formed between the photoactive layer and the cathode yields a built-in potential defined by the difference between the Fermi level of the BHJ E_{Fp} and the effective cathode work function $\Phi_{cathode}$. The observed changes in V_{BI} are reflected in the magnitude of the change in V_{OC}. Furthermore, EQE data reveal the overall device performance enhancement to be due entirely to the inclusion of the surfactant, rather than a beneficial change in photoactive layer morphology.

Device	V_{OC} [V]	J_{SC} [mA cm^{-2}]	FF	PCE [%]	R_{SH} [Φ cm^{-2}]
Al	0.619	10.28	0.51	3.22	309
Al/C_{60}-bis	0.877	11.19	0.60	5.87	773
Ag	0.734	10.83	0.53	4.22	351
Ag/C_{60}-bis	0.879	11.50	0.61	6.22	663
Cu	0.672	9.58	0.51	3.32	387
Cu/C_{60}-bis	0.875	10.13	0.61	5.37	795

Table 2-1: Summary of performance data for PhanQ:$PC_{71}BM$ devices with different cathode metals, with and without C_{60}-bis.

Device	V_{OC} [V]	V_{BI} [V]	(ΔV_{OC}, ΔV_{BI}) [V]	N [10^{16} cm^{-3}]	w [nm]	$\Phi_{cathode}$ [eV]
Al	0.619	0.636	-	2.25	97	4.25
Al/C_{60}-bis	0.877	0.940	(0.26, 0.30)	3.32	97	3.66
Ag	0.734	0.808	-	3.39	89	4.57
Ag/C_{60}-bis	0.879	0.959	(0.15, 0.15)	3.77	92	3.97
Cu	0.672	0.712	-	2.51	97	4.70
Cu/C_{60}-bis	0.875	0.957	(0.20, 0.25)	4.02	89	3.96

Table 2-2: Summary of the built-in potential V_{BI}, dopant concentration N, and depletion width w of the organic/cathode Schottky contact from Mott-Schottky analysis. The work functions and relative shifts in V_{OC} and V_{BI} for all devices are also included.

CHAPTER 3:
Probing recombination dynamics with impedance spectroscopy

3.1 Introduction

The rapid pace of development of photoactive layer materials has led to new benchmark device efficiencies, however the increasing complexity of polymer and fullerene structures necessarily translates to a more complex nanoscale structure in a completed device. Several recent papers have identified bimolecular recombination as a key loss pathway in OSC.[30–35] While it has been explicitly mentioned in almost all of these studies that the active layer morphology plays an important role in determining device parameters in general and the strength of bimolecular recombination in particular, the majority of them describe the use of purely electrical and/or optoelectronic methods, and there exist very few structural data that adequately support this claim. In this chapter, we describe the use of impedance spectroscopy to simultaneously probe charge recombination lifetimes and DOS distributions in high performance solar cells with a wide range of photoactive layer compositions, and further provide morphological data obtained from grazing-incidence small-angle x-ray scattering (GISAXS). We show that there is a correlation between decreased device performance, a strongly altered DOS profile and arrested aggregation of fullerene molecules in the photoactive layer.

3.2 Impedance spectroscopy and its application to organic solar cells

3.2.1 Introduction to impedance spectroscopy

Generally speaking, impedance spectroscopy consists of measuring the AC electrical current response of a system to which a small signal, AC voltage perturbation of frequency ω is applied.[36] Typically, a perturbation amplitude of no more than a few tens of mV is applied in order to maintain the linearity of the system response. Various processes in solid-state solar cells respond to stimuli in different frequency regimes, hence an impedance spectrum is usually measured over a broad frequency range from mHz to MHz.[37] Indeed, when the probe frequency is small, the system response approaches that of steady state conditions. As the frequency is increased, other faster processes are more strongly activated, however the impedance response will contain contributions from all processes. This method offers an advantage over transient time-domain methods, wherein a small amplitude perturbation is applied and the system is observed as it tends toward equilibrium. The time-domain decay resulting from the perturbation usually has some characteristic time constant τ, and in the case where the system is governed by only one decay process, it can be shown the impedance spectroscopy and transient decay methods are both valid. However, if the system response is composed of many different processes all happening simultaneously, it is difficult to resolve the different time constants that make up the transient decay. By applying an appropriate equivalent electrical circuit to impedance spectra, one can effectively deconvolute the overall system response and gain some insight into the individual processes. It most be noted here that this approach necessitates some prior knowledge of how the system might be modeled.[36,37] It can be shown that equivalent circuits are, in general, not unique. In fact, many circuit models may give the exact same impedance response over the frequency range of interest, which can lead to misinterpretation of

the parameters extracted from fitting the data.[38] Another potential pitfall lies in the potentially infinite complexity of an equivalent circuit; similar to fitting a polynomial with an arbitrarily large number of terms, the experimentalist may find excellent fit statistics with an arbitrarily complex equivalent circuit, but only a few of those circuit parameters may have any real physical meaning. With these caveats in mind, it is usually useful to choose the simplest model applicable to the system under study.

3.2.2 The chemical capacitance and density-of-states

When we speak of capacitance, we are usually describing the classical electrostatic example of a geometric capacitance set up between two parallel plates with equal amounts of opposite charge separated by some distance. As the scale of the plates is decreased, this picture is no longer generally valid, and we must take the plates and the "electron reservoirs" to which they are connected as an indivisible unit.[39,40] This changes the relevant capacitance from purely geometrical, given by $C_g = dQ/dV$, to electrochemical, given by $C_\mu = qdQ/d\mu$, where q is the electron elementary charge and μ is the chemical potential. In this picture, the chemical capacitance relates the accumulated charge on the opposite plates to a difference in the chemical potential of the electron reservoirs, which means that the DOS of the capacitor plates contributes to the overall capacitance as $C_{DOS} = q^2 dN/dE$. In the macroscopic case, where dN/dE of the plates is very large, C_{DOS} can be ignored and the total capacitance reduces to the aforementioned purely geometrical value.

This concept can be readily applied to the case of OSC, where the two "plates" of the capacitor are taken as the polymer and fullerene domains in contact with their respective contacts. From a thermodynamic standpoint, a capacitor stores energy in a volume element by means of a generalized displacement.[40] The chemical capacitance then describes the ability of a

system to accept and lose charge carriers with a density N_i due to a change in their potential μ_i. We write the chemical capacitance per unit volume as:

$$(1) \qquad C_\mu^{(i)} = \frac{q^2 \partial N_i}{\partial \mu_i}$$

We equate μ_i with the electron Fermi level E_{Fn} and obtain the chemical capacitance of electrons occupying the fullerene LUMO manifold:

$$(2) \qquad C_\mu^{(n)} = \frac{q^2 \partial n}{\partial E_{Fn}}$$

Due to the inherently complex nature of the BHJ photoactive layer, the polymer HOMO and fullerene LUMO DOS distributions are expected to tail significantly into the effective polymer/fullerene bandgap.[31,41,42] This has the effect of localizing a density of electrons n_L into the "trapping" tail states of the bandgap DOS $g_n(E_{Fn})$. Integrating over the bandgap yields the value of n_L, and invoking the Fermi-Dirac distribution gives:

$$(3) \qquad n_L = \int_{E_{HOMO}}^{E_{LUMO}} g_n(E) f(E - E_{Fn}) dE$$

In the zero temperature limit of the Fermi-Dirac distribution, occupancy of the localized tail states would begin at E_{Fn} and would be zero above. Hence we arrive at a simplified expression of the chemical capacitance:

$$(4) \qquad C_\mu^{(trap)}(E) = \frac{q^2 \partial n_L}{\partial E_{Fn}} = q g_n(E_{Fn})$$

Under steady-state illumination conditions, it is possible to extract the chemical capacitance values from equivalent circuit fits to impedance spectra when the perturbation signal is superimposed on a DC bias equal to the intensity-dependent $V_{OC}(I)$. In this case, the measured chemical capacitance is a result of the intensity modulated quasi-Fermi level splitting obtained via population of the fullerene LUMO tail states by excess photogenerated electrons, and a plot of C_μ vs. $V_{OC}(I)$ produces an estimate of the electron DOS profile.

3.2.3 The recombination resistance

Another important parameter obtained from impedance spectroscopy is the recombination resistance (R_{rec}). Neglecting losses due to series and shunt resistances, J-V curves in BHJ OSC can be characterized by:

$$J = J_O \left[exp\left(\frac{q\beta V_{OC}}{k_b T}\right) - 1 \right] - J_{ph} \quad (5)$$

where J_O is the saturation current under reverse bias, J_{ph} is the photocurrent and β is the inverse of the diode ideality factor.[41,43] When transport resistance and contact effects do not limit the device current, the first summand is taken as the recombination current J_{rec} and R_{rec} is given by:

$$R_{rec} = \left(\frac{dJ_{rec}}{dV_{OC}}\right)^{-1} \quad (6)$$

which describes the current flow as charges in the fullerene LUMO recombine with holes in the polymer HOMO. As with the chemical capacitance, recombination resistance is readily extracted by appropriate fitting of impedance spectra. While the recombination resistance can often provide information regarding the kinetics of recombination in OSC, it is the lifetime product of R_{rec} and C_μ, τ that is of paramount importance and will be the focus of our discussion in the next section.

3.3 Experimental details

Devices with the structure Glass/ITO/PEDOT:PSS/x-PhanQ:$PC_{71}BM$/C60-bis/Ag were processed from 20 mg/ml solutions stirred overnight, and held throughout spin-coating, at 80˚C. After several iterations of this experiment, it was observed that the C60-bis no longer properly wet the active layer while spin-coating under ambient conditions. It was hypothesized that this

was due to the relative humidity and residual solvent vapor conditions in the fume hood where the spin-coater was located, and so a solution was prepared at the same concentration in dry methanol for deposition in the glovebox. This completely alleviated the dewetting problem, and was thereafter adopted as standard procedure.

Devices in which the composition was varied by changing the nature of the fullerene had the structure Quartz/MoO_3/Ag/MoO_3/PhanQ:fullerene/Ca/Al. These devices were prepared as part of a collaboration involving morphological characterization by grazing incidence small angle neutron scattering (GISANS), which placed experimental constraints on the nature of the substrate and bottom contact. In order to obtain unadulterated scattering data, the substrate could not contain boron impurities usually found in glass/ITO substrates nor any undue scattering centers such as those found in thermally cured layers of PEDOT:PSS. Firstly, the quartz substrates were carefully diced so as to achieve a reproducible device area. They were then cleaned as the glass/ITO substrates from Section 2-3 and transferred into a thermal evaporation chamber. MoO_3 was evaporated to a thickness of 40 nm at a rate of 0.2 Å/s, followed by Ag with a thickness of 15 nm at a rate of 5 Å/s and finally another layer of MoO_3 with a thickness of 5 nm at the same rate as the first layer. Before spin-coating the active layer a small dot of indium metal was affixed to the composite anode far from where the cathode contact would be evaporated. Solutions were prepared at a concentration of 20 mg/ml (1:3 PhanQ:fullerene by weight) by stirring overnight at 80˚C in a glovebox. The solutions were cooled to room temperature and filtered before spin-coating at 800 RPM for 120 s, then immediately at 2000 RPM for 5 s to remover excess solution from the substrate edges. The devices were then annealed at 110˚C for 10 min before being transferred into the evaporation chamber. Ca/Al electrodes were deposited through a shadow mask in such a way that the overlap of the top

contact with the underlying composite anode described above defined a device active area of 4.64 mm^2.

J-V characterization was carried out with a Keithley 2400 source meter in a N_2 glovebox equipped with a quartz window to allow AM1.5G illumination by a Solar Light 16S-300 W solar simulator (Xe lamp). The light intensity was calibrated as in Section 2-3. The center conductors of two independent coaxial cables were used to carry the DC output of the source meter to the device via BNC feed-throughs in the glovebox. A Hewlett-Packard HP4284A LCR meter with a 4-into-2 terminal configuration was used to obtain light intensity dependent impedance spectra. The instrument's open and short circuit correction settings were used to account for stray L, R and C caused by contacts and leads. A 1 m cable length correction factor was also applied, although it is noted that the actual distance from the instrument reference plane to the device was longer than 1 m. A dual-wheel filter assembly equipped with neutral density filters was employed to change the light intensity incident upon the device. The light intensity could be tuned over a wide range from 100 mW/cm^2 down to 0.01 mW/cm^2. The light intensity-dependent V_{OC} values were obtained just prior to measuring the intensity dependent impedance spectra for the same device. At each light intensity setting, an AC perturbation voltage of 20 mV and a DC bias equal to V_{OC} were applied to the device over a frequency range of 200 Hz to 1 MHz, with 50 points per scan. The instrument was operated in the Z-θ (radian) mode and set to perform 5 analogue-to-digital conversions per frequency point, with an integration time set to "short".

3.4 Results and discussion

3.4.1 Fluorine-substituted PhanQ:$PC_{71}BM$ devices

The design concept of PhanQ was originally motivated by the desire to simultaneously decrease the polymer bandgap, which would allow for better overlap of the solar spectrum with the polymer's absorption profile, and increase the V_{OC}. The strong interaction between the donor and acceptor moieties of the polymer backbone makes it possible to decrease the bandgap without sacrificing V_{OC} by, for example, upshifting the polymer HOMO level.[24] By further modifying the PhanQ with electron withdrawing groups, it would be possible to increase the V_{OC} without widening the bandgap by virtue of downshifting both the HOMO and LUMO of the polymer in approximately equal measure. To this end, several fluorinated PhanQ derivatives were synthesized, the chemical structures of which are shown in Figure 3-1. Based on the energy level data (Table 3-1) one would expect a trend in V_{OC} like DiF(b)-PhanQ > F-PhanQ > DiF(t)-PhanQ > PhanQ, and indeed the J-V data bear this out. Figure 3-2 shows the linear J-V curves for a representative set of devices, the parameters for which are summarized in Table 3-2.

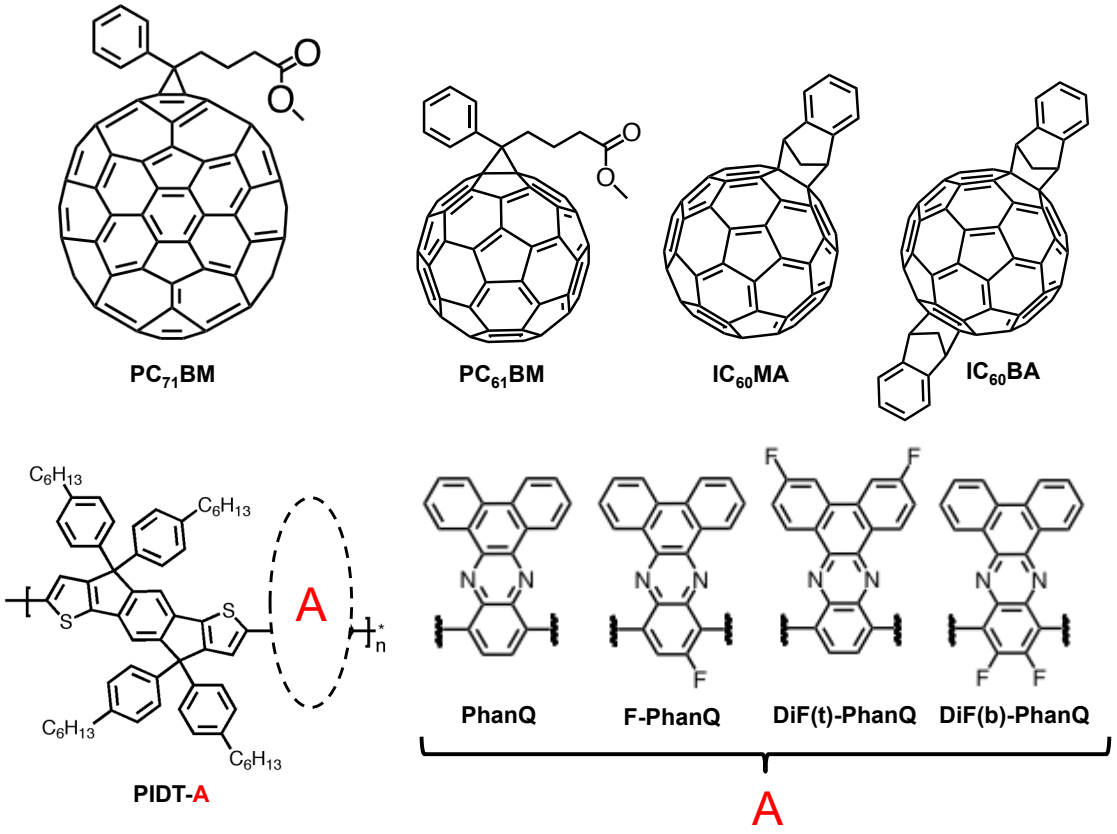

Figure 3-1: Chemical structures of the materials used in this work. Devices are typically fabricated in a 3:1 weight ratio of a fullerene (top row) and a polymer (bottom row). Polymers were synthesized with a variety of acceptor moieties, denoted A, in order to tune the energy levels for enhanced V_{OC} while maintaining essentially the same absorption profile.

It should be noted that batches of devices often deviated from this trend due to variations in device quality, however the impedance spectra and subsequent extraction of recombination parameters were only dependent on biasing the device at V_{OC}, rather than on its absolute magnitude. In other words, the same recombination resistance and chemical capacitance data were obtained across many iterations of the experiment, even though the maximum achievable V_{OC} (at 1 sun) varied. This is then a good indication that the processes being probed were indeed related only to the bulk.

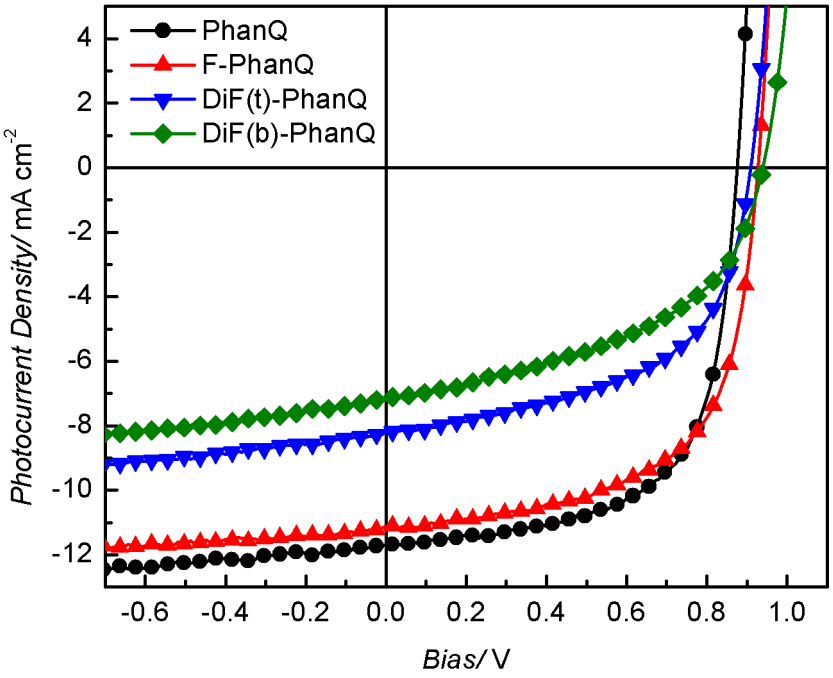

Figure 3-2: J-V curves at 1 sun illumination conditions for the x-PhanQ polymer:$PC_{71}BM$ devices tested. A marked decrease in photocurrent in the case of DiF(t)- and DiF(b)-PhanQ is attributed to a suboptimal driving force for exciton charge separation.

Figure 3-3 shows a typical series of light intensity dependent impedance spectra for PhanQ devices plotted in the complex plane (Cole-Cole plot). The spectra are characterized by a major RC arc related to charge recombination,[44–46] while a smaller and less obvious arc shows up at higher frequency, and has been attributed to the R and C elements associated with interfaces involving the outer contacts. A rather complicated equivalent circuit has recently been proposed wherein a geometric capacitance in parallel and a transport resistance in series with the recombination $R_{rec}C_{\mu}$ subcircuit are utilized.[47] We note that this circuit is only valid under the experimental conditions used therein; namely that the transport resistance and geometric capacitance only appear when the DC bias is varied at constant illumination. The fitting software we used for analysis in our experiment uses a simple statistical discrimination process to determine whether or not a particular circuit element is valid. Essentially, the error in an element value is calculated by testing a number of possible solutions larger and smaller than the

"best fit" value. The deviation from this value is increased until the weighted sum of squares, which is proportional to the average percent error between the experimental and analytical values of the model, begins to increase. Large circuit element error values are a good indication that the element is not relevant to the model, and can be removed from the circuit entirely. Including the aforementioned geometric capacitance and transport resistance in our circuit model yielded very large error estimates and were thus excluded, which makes sense intuitively, since the dominant processes at open-circuit are the photogeneration and subsequent recombination of charge carriers.

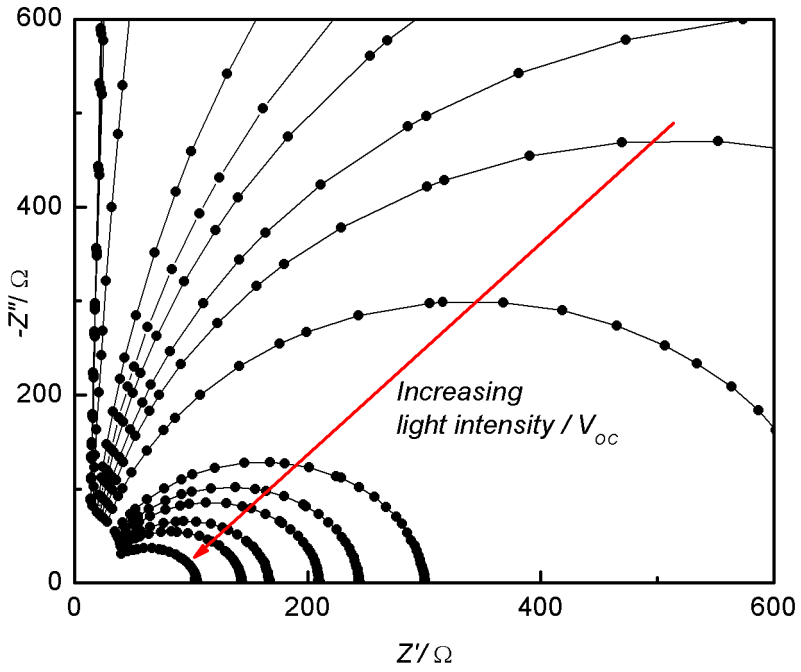

Figure 3-3: Light intensity-dependent impedance spectra of a PhanQ:$PC_{71}BM$ device biased at V_{OC}, represented as the negative imaginary versus real components of the complex impedance Z(ω) (Cole-Cole plot). Parallel RC circuit elements appear in the plot as semicircles. Typical impedance spectra for the devices studied here are dominated by a large RC arc at lower frequencies (frequency increases right to left along arc), which indicates the chemical capacitance and recombination resistance related to charge recombination.

In Figure 3-4 we show the R_{rec} and C_{μ} values extracted from fitting the impedance spectra for all four polymer:fullerene blends. Solid lines representing exponential fits to the data are shown in both plots with the corresponding equations:

(7) $$R_{rec} = R_o \exp\left(-\frac{q\beta V_{OC}}{k_b T}\right)$$

(8) $$C_\mu = C_o \exp\left(\frac{q\alpha V_{OC}}{k_b T}\right)$$

We note that for all polymers, R_{rec} begins to saturate at low charge carrier density toward the RC limit of the device. This has been attributed to the relatively small shunt resistances of the devices under study, arising from variations in processing quality.[48] At low charge density the effective resistance of the device is quite large and the charges will tend discharge through the lowest resistance pathway. Nevertheless, it is the higher intensity, higher charge carrier density regime we focus on for our impedance analysis.

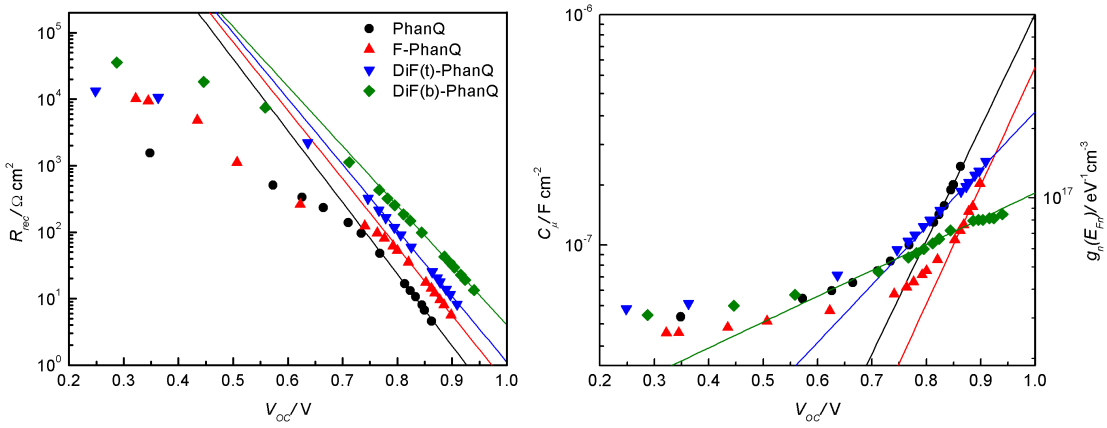

Figure 3-4: (left) Recombination resistance and (right) chemical capacitance values extracted from impedance spectra and plotted against their respective light intensity-dependent V_{OC} values. Solid lines are exponential fits to the high intensity data. The chemical capacitance plot includes a second y-axis scaled by application of Equation 4.

In a recent work, the recombination parameter β and DOS tailing parameter α were empirically related through the recombination current density J_{rec} for devices composed of poly(3-hexylthiophene) (P3HT) and various fullerenes.[43] It was shown that J_{rec} is proportional to the square of the excess photogenerated electron density, which in turn is proportional to exp(-$q\beta V_{OC}/k_bT$) and exp($2q\alpha V_{OC}/k_bT$). This proportionality allowed the authors to state that $\beta=2\alpha$, which was born out empirically by fitting of their impedance spectra. Our data reflect the same empirical relationship for PhanQ and F-PhanQ, but begin to deviate significantly for the two

DiF-PhanQ polymers (Table 3-2). It must be noted that this recombination model makes the assumption that any electron occupied state in the fullerene phase is able to transfer to any vacant state in the polymer with a probability dependent on the electron and hole quasi-Fermi levels of the recombining carriers. Furthermore, the model does not make any statements about the spatial distribution of charge carriers, rather we are measuring an averaged Fermi level over the entire bulk, which does not allow us to explicitly state, for example, the distance of a recombining electron from the polymer/fullerene interface.[43] The possibility of different recombination pathways simultaneously affecting the recombination kinetics in different blends may explain the aforementioned deviation from $\beta=2\alpha$. In Figure 3-5 we show the recombination lifetimes each different blend calculated from their respective impedance parameters. In the higher light intensity regime, we see a linear relationship between the recombination lifetime and the charge density calculated by integration of the chemical capacitance. By linearly fitting a log-log plot of the same data, we are able to extract a slope parameter γ that directly relates the carrier recombination kinetics with carrier density as $\tau \propto n^{-\gamma}$. It has been proposed that $\gamma=2$ indicates bimolecular recombination kinetics, however we observe values of γ greater than two, indicating a higher order dependence of lifetime on charge carrier density. It should be mentioned that this behavior is not unprecedented, and has been observed in transient lifetime analyses.[33,49]

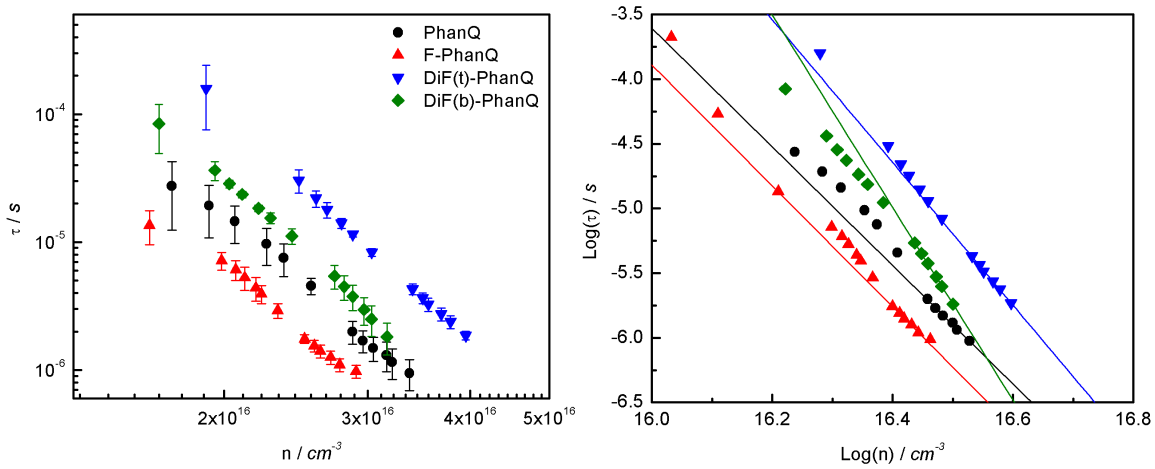

Figure 3-5: (left) Recombination lifetime $\tau=R_{rec}C_{\mu}$ versus charge density obtained by integration of the C_{μ} curves in Figure 3-4. Error bars indicate +/- one standard deviation for data averaged over three iterations of the same experiment (i.e. one device on three separate substrates per polymer). (right) Log-log plot of the same data, excluding error bars for better visualization. An steeper slope (larger γ) in the log-log plot qualitatively describes the adverse effects of a broadened DOS as it tails further into the bandgap.

We hypothesize that morphology plays an important role in determining the shape of the electron DOS and therefore the relation of carrier lifetime to increasing DOS occupancy. To test this hypothesis, we obtained GISAXS profiles for four polymers blended with $PC_{71}BM$ (Figure 3-6).[50] We observe greater scattering intensity at larger values of Q_y (off-specular scattering) for DiF(t)-PhanQ compared to all other polymers in the series. We interpret these data as indicating a large degree of small aggregates of $PC_{71}BM$ in the bulk. Smaller aggregates typically mean a higher surface-to-volume ratio, and hence an increase in polymer/fullerene interfaces where recombination can occur. At the same time, a less aggregated, more spread out fullerene phase with a higher solubility in the polymer phase of the BHJ would yield a broader electron DOS distribution in the bandgap.

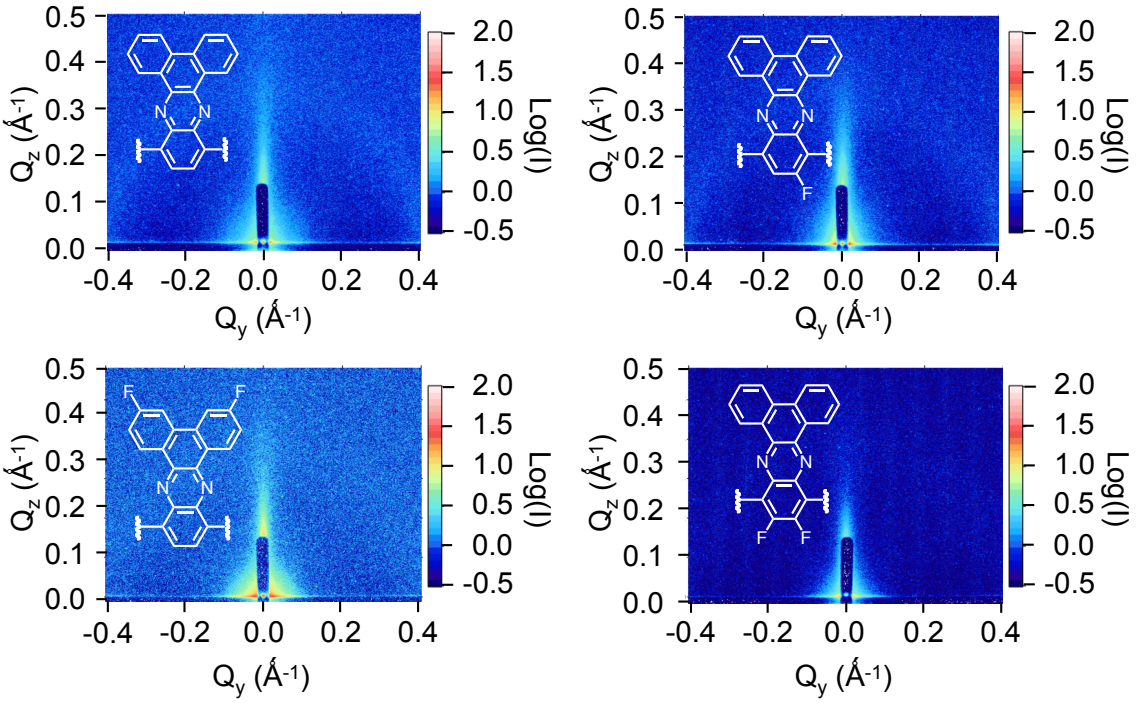

Figure 3-6: GISAXS profiles for the x-PhanQ:$PC_{71}BM$ blends plotted in reciprocal space. The Q_z axis shows the orthogonal scattering (specular) of the incident x-ray beam while Q_y represents the in-plane scattering component. A wider intensity profile in the Q_y axis is indicative of smaller fullerene aggregates.

This is supported by the α parameters mentioned previously in that a smaller α indicates a broader DOS with a higher degree of tailing into the bandgap. From Figure 3-5, it is clear that the only polymer that deviates from this observation is DiF(b)-PhanQ. Although α is significantly lower in this case than in any other system, the GISAXS profile we obtained shows even less off-specular scattering than PhanQ and F-PhanQ, suggesting the absence of small fullerene aggregates, which in turn suggests that the apparent broadening of the DOS is unrelated to the film morphology. We have previously studied charge transfer energetics of these polymer:fullerene blends by photoinduced absorption spectroscopy (PIA)[50] and found that the driving force for exciton dissociation is below the threshold for spontaneous free charge carrier generation for DiF(b)-PhanQ, which is distinctly different from any of the other three polymers under study. It is not unreasonable to assume that, due to an inherently different energy landscape for this polymer, we could expect to see a vastly different DOS distribution as well.

The exact nature of this difference relative to the lifetime behavior observed for the other polymers is as yet unresolved, and warrants further investigation.

3.4.2 PhanQ:C_{60} fullerene devices

In order to verify the generality of the above assertion, that carrier lifetimes are related to morphology through the DOS, we fabricated BHJ devices composed of PhanQ blended with various C_{60} fullerenes (Figure 3-1). Figure 3-7 shows the J-V curves of the devices under 1 sun illumination conditions. The device parameters, summarized in Table 3-2, indicate little difference in performance between the $PC_{61}BM$ and $IC_{60}MA$ cases but a rather large increase in V_{OC} for $IC_{60}BA$. The differences in V_{OC} roughly correspond to the cyclic voltammetry deduced LUMO levels of the three fullerenes,[51] however $IC_{60}BA$ suffers from a significantly reduced FF and PCE compared to $PC_{61}BM$.

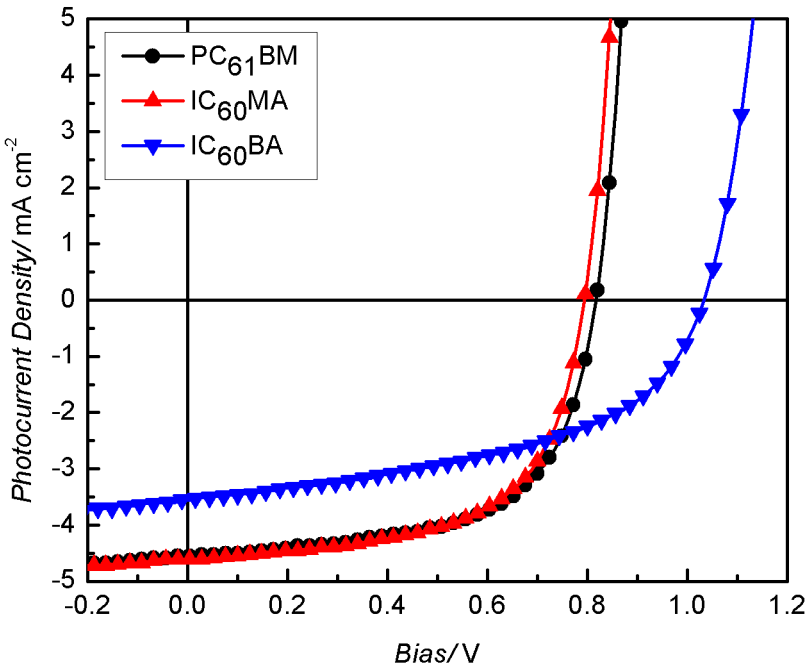

Figure 3-7: Representative J-V curves at 1 sun illumination conditions for the PhanQ:C_{60} fullerene devices. A large increase in V_{OC} for $IC_{60}BA$ is due to an upshifted LUMO, which acts to increase the quasi-Fermi level splitting. The decrease in photocurrent density is attributed to a combination of poor exciton dissociation driving force and poor morphology, as indicated by the DOS extracted from impedance spectroscopy as well as enhanced small-angle scattering intensity from GISAXS analysis.

Figure 3-8 shows the recombination resistance and chemical capacitance/DOS data extracted from IS measurements of the different fullerene blends. As with the F-substituted PhanQ polymer series, all three fullerenes show the same dependence of R_{rec} on V_{OC} with β values in the range of 0.55 to 0.61, however the difference in chemical capacitance behavior between them is quite dramatic. By inspection $PC_{61}BM$ and $IC_{60}MA$ appear to have very similar DOS distributions, and indeed they both have an α value of 0.30. As before, a linear fit to the log-log plot of lifetime vs. carrier density indicates that the devices exhibiting similar α also have similar recombination dynamics, while the significantly lower α $IC_{60}BA$ case exhibits a much sharper drop in lifetime vs. charge density. Figure 3-9 shows GISAXS and lifetime data for the different fullerene blends. We observe markedly increased off-specular scattering intensity for the $IC_{60}BA$ device, but very little if any such behavior for the other two fullerenes.

We conclude that the correlation between poor morphology, broadened DOS distribution and shorter lifetime with increased occupancy, previously proposed for the F-substituted PhanQ polymer series, is supported here with entirely different active layer compositions.

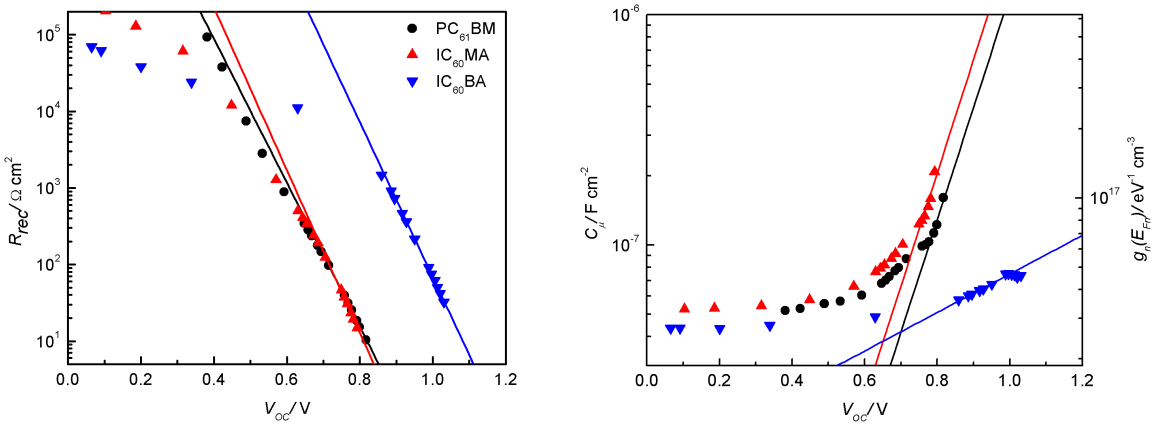

Figure 3-8: (left) Recombination resistance and (right) chemical capacitance data for PhanQ:C_{60} fullerene devices analyzed as in Figure 3-4.

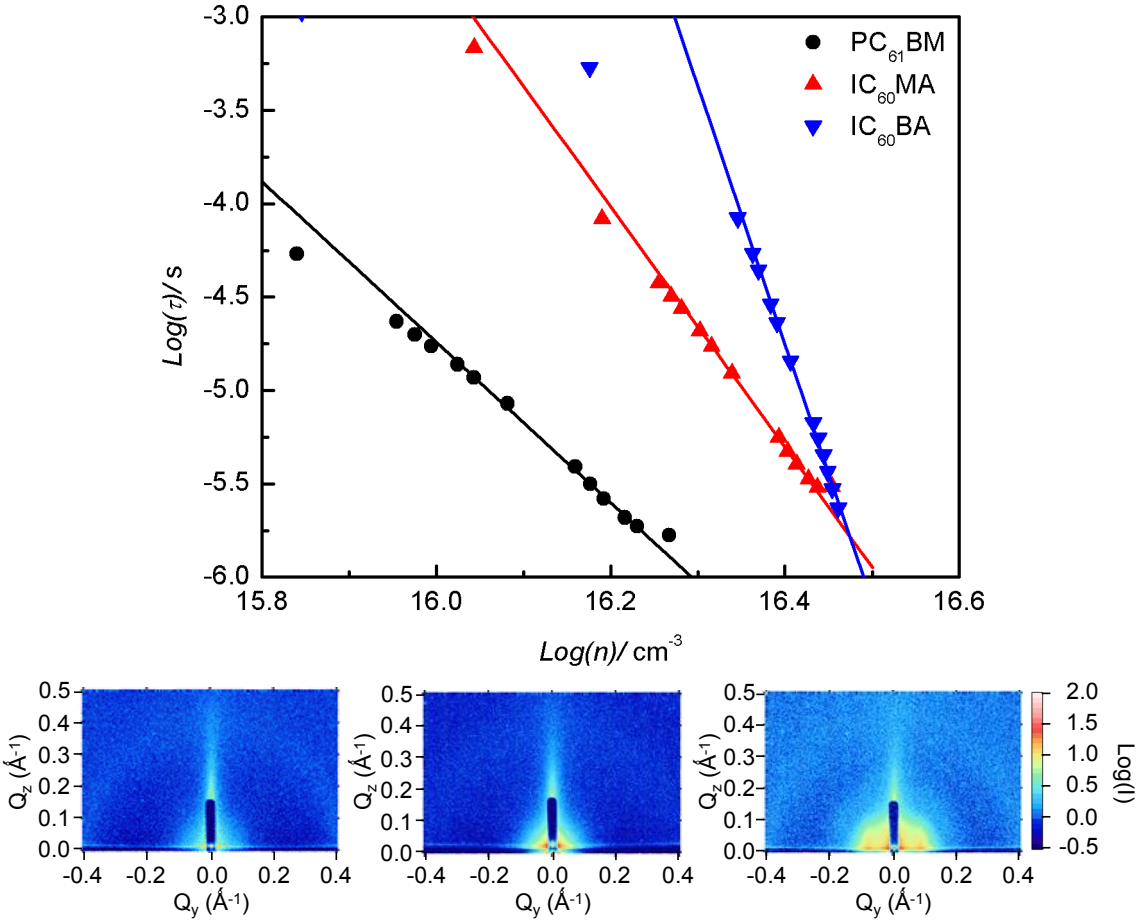

Figure 3-9: Recombination data for PhanQ:C_{60} fullerene devices with linear fits through the high light intensity points, and (bottom) corresponding GISAXS profiles. From left: $PC_{61}BM$, $IC_{60}MA$ and $IC_{60}BA$. $IC_{60}BA$ shows behavior qualitatively similar to devices composed of DiF(t)-PhanQ and $PC_{71}BM$.

Material	*HOMO* *[eV]*	*LUMO* *[eV]*
PhanQ	5.10	3.36
F-PhanQ	5.16	3.40
DiF(t)-PhanQ	5.14	3.48
DiF(b)-PhanQ	5.22	3.44
$PC_{61}BM$	-	4.30
$IC_{60}MA$	-	3.86
$IC_{60}BA$	-	3.74

Table 3-1: Summary of material energy levels obtained by cyclic voltammetry. LUMO levels for fullerenes were calculated from the onset of the first reduction potential against ferrocene. LUMO levels for polymers were measured in a similar fashion, while the HOMO levels were calculated by adding energy corresponding to the low photon energy onset of UV-Vis absorption spectra.

Device	V_{OC} *[V]*	J_{SC} *[mA cm^{-2}]*	*FF*	*PCE* *[%]*	α	β	2α	γ
PhanQ	0.876	11.67	0.65	6.62	0.31	0.62	0.62	4.58
F-PhanQ	0.928	11.11	0.62	6.42	0.32	0.63	0.64	4.67
DiF(t)-PhanQ	0.909	8.20	0.55	4.12	0.15	0.61	0.30	5.65
DiF(b)-PhanQ	0.940	7.17	0.48	3.22	0.06	0.56	0.12	7.45
$PC_{61}BM$	0.817	4.53	0.61	2.28	0.30	0.55	0.60	4.29
$IC_{60}MA$	0.794	4.61	0.60	2.21	0.30	0.59	0.60	6.44
$IC_{60}BA$	1.03	3.55	0.49	1.81	0.05	0.61	0.10	13.83

Table 3-2: Summary of J-V device characteristics and slope parameters extracted from impedance spectroscopy analysis for all devices.

CHAPTER 4:
Conclusions and future directions

4.1 Conclusions

We have studied the device physics of bulk-heterojunction organic solar cells incorporating various materials aimed at engineering interfaces within completed devices. In one line of investigation, we synthesized a C_{60} bis-adduct surfactant to be used as a buffer between the photoactive layer and the thermally evaporated metal top contact of a conventional structure organic solar cell. By systematically varying the work function of the contact metal, with and without the surfactant buffer layer, we gained insight into the physics governing the photoactive layer/metal interface and vastly improved the device performance. By applying Mott-Schottky analysis to the capacitance-voltage data obtained for these devices we were able to conclude that the surfactant modifies the metal work function to an appreciable extent, and allows for efficient charge extraction and significantly enhanced open-circuit voltage regardless of the chosen contact metal. This aspect allowed us to use more air-stable metals that would ordinarily be prohibited due to suboptimal energy level alignment at the electron-collecting electrode. In a second investigation we used impedance spectroscopy to probe charge carrier recombination dynamics at the donor polymer/acceptor fullerene interface in devices composed of PhanQ, as well as its fluorinated derivatives, and various fullerenes. We found that the morphology of the blended photoactive layer had a strong influence on the electronic DOS distribution, which in turn directly affected the recombination rate as well as the achievable V_{OC}.

We show that attempting to increase the open-circuit voltage through structurally tuning the LUMO level of the fullerene inadvertently introduces different polymer/fullerene phase separation that leads to a reduction in photocurrent. We observe that the recombination lifetime drops off more steeply with increasing excess photogenerated charge density for blends with more finely separated phases and propose that the resulting increase in recombination surface area leads directly to reduced overall device performance, despite a marked increase in open-circuit voltage.

4.2 Future directions

In Chapter 3 we noted a strong correlation between apparent differences in active layer morphology, brought about by incorporating different photoactive materials, and the dependence of charge carrier recombination lifetime on density of excess photogenerated carriers. It must be noted that the GISAXS data presented in this dissertation, while encouraging, are preliminary. Analysis of GISAXS profiles is non-trivial and is based on a number of variable factors including scattering center number density, scattering volume and length, aggregate form factors and a spatial correlation factor, to name a few. Going forward, we wish to know more about the nature of the size and spatial distribution of fullerene aggregates in bulk-heterojunction layers, with the ultimate goal of correlating recombination dynamics to a well-known set of morphological parameters. By carefully tuning materials properties of polymers and fullerenes and observing their morphological differences, we hope to be able to predict a device's performance and recombination dynamics based solely on the knowledge of how the materials interact with each other in the bulk film. This in turn would afford us yet another tool for rational design of the next generation of polymers and fullerenes for OSC.

At present, we can say with certainty that the choice of photoactive layer materials has a strong influence on the final device morphology, and that it is reasonable to assume that some polymers are responsible for driving the growth of smaller fullerene aggregates. Whether it is the fullerene size distribution, the spacing or some combination of the two that we're observing in GISAXS remains an open question. We propose that gaining some insight into the solubility of fullerenes in the polymer matrix, perhaps by spectroscopic ellipsometry, is an important first step to decoupling the aforementioned host of morphological variables, which would bring us more clarity in our interpretation of GISAXS data.

It was observed that subtle differences in device processing lead to sometimes significant changes in the recombination lifetime behavior obtained through impedance spectroscopy analysis. Though there was adequate statistical agreement between different iterations of the experiment, indicated by the error bars in Figure 3-5, we suggest that future studies include a greater number of devices from the same substrate to further reduce statistical anomalies in the data. The acquisition of impedance spectra is, at present, highly serial and manual in nature. Automation of the neutral density filter apparatus, inclusion of a shutter and a Peltier cell to control substrate temperature are all possible improvements that could be made to the experimental setup. Nevertheless, impedance spectroscopy is proving to be a valuable tool in simultaneously evaluating several important device performance metrics of organic solar cells.

APPENDIX A:
Appendix to CHAPTER 2

A.1 Cyclic voltammetry measurements

Cyclic voltammetry measurements were carried out under N_2 in a one-compartment cell equipped with a glassy carbon working electrode, a platinum wire counter electrode, and a Ag/Ag^+ reference electrode. Measurements were performed in THF solution containing Tetrabutylammonium Hexafluorophosphate (0.1 **M**) as a supporting electrolyte with a scan rate of 100 mV/s. All potentials were corrected against the Fc/Fc^+ couple and LUMO levels were estimated using the following equation: LUMO = -(4.8 + $E_{1/2}^{red1}$) eV.

A.2 Work function measurements

Work function values were obtained following a modified method previously employed by Professor Rudy Schlaf's research group at the University of South Florida (M.M. Beerbom et al., *Journal of Electron Spectroscopy and Related Phenomena* 152, **2006**, 12-17). The spectrometer's analyzer was calibrated according to the manufacturer's guidelines to yield photoemission lines of Ar^+ ion sputter-cleaned copper and gold foils for Cu 2p 3/2 and Au 4f 7/2 at 932.62 eV and 83.96 eV, respectively, following ISO 15472 (M.P. Seah, *Surf. Interface Anal.*, 31, **2001**, 721-723). This procedure ensures the linearity of the binding energy scale for the instrument,

extrapolated out to the secondary electron cutoff (SEC) near the photon energy of the system (1486.6 eV for monochromated Al K-α x-rays). SEC spectra were measured at an x-ray power of 25W and 15kV acceleration at normal emission (90˚ take-off angle). For all SEC spectra a bias of -15V was applied during measurement to ensure ample separation of the sample SEC and that of the analyzer. Under these conditions a SEC value of 1466.24 eV for clean, polycrystalline gold was obtained, corresponding to a work function of 5.36 eV. Since the Cu and Au core level spectra mentioned above are referenced to the Fermi level, set at zero binding energy, the work function of gold was obtained by $\Phi_{gold} = (h\upsilon - qV_{app} - E_{SEC})$ where $h\upsilon$ is the x-ray photon energy, V_{app} is the applied bias and E_{SEC} is energy position of the secondary electron cutoff on the binding energy scale. Ideally, the SEC edge should be a step function at 0K, however experimental conditions include thermal and instrumental broadening. Hence, the position of the SEC is taken as the local maximum of the first derivative of the SEC feature. Figure S1 below shows the SEC spectrum of clean, polycrystalline Au foil and its corresponding first derivative. Once the work function of clean Au has been obtained thusly, all other sample work functions can be derived simply from their SEC positions obtained via the first derivative method as $\Phi_{sample} = (E_{SEC,\,gold} - E_{SEC,\,sample}) + \Phi_{gold}$. Figure S2 shows the SEC spectra for Al, Ag and Cu with and without C_{60}-bis. Figure S2c includes the SEC spectrum of clean gold foil as a reference.

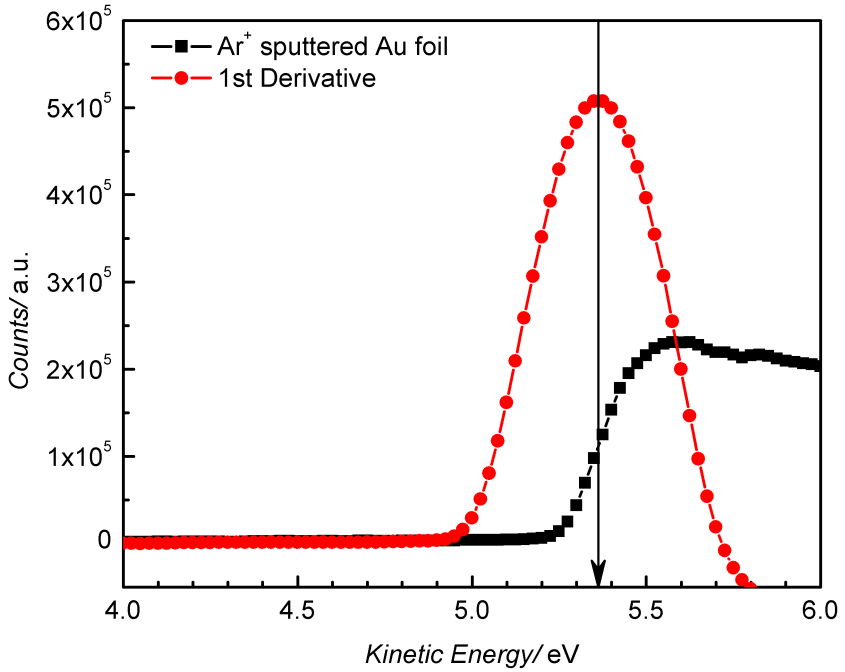

Figure A-1: Secondary electron cutoff spectrum and first derivative of Ar^+ ion sputter-cleaned gold foil represented on the kinetic energy scale. The vertical line through the center of the first derivative is a guide for the eye such that the work function may be read directly off the kinetic energy scale.

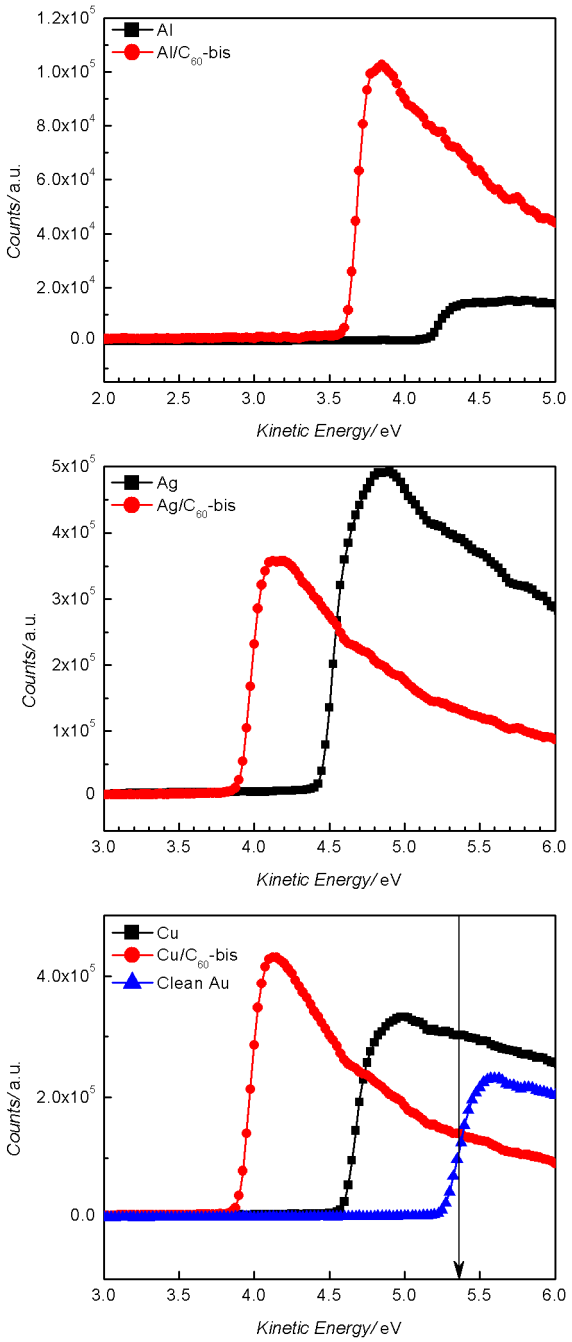

Figure 4.2: Secondary electron cutoff spectra of (from top) Al, Ag and Cu metal films with and without C_{60}-bis. Films without C_{60}-bis were Ar^+ sputter-cleaned in vaccuo prior to measurement to ensure an accurate work function. The Cu spectrum includes that of clean Au foil as a reference.

BIBLIOGRAPHY

1. Dennler, G., Scharber, M. C. & Brabec, C. J. Polymer-Fullerene Bulk-Heterojunction Solar Cells. *Adv. Mater.* **21,** 1323–1338 (2009).
2. Krebs, F. C. Fabrication and processing of polymer solar cells: A review of printing and coating techniques. *Sol. Energy Mater. Sol. Cells* **93,** 394–412 (2009).
3. Liang, Y. *et al.* For the Bright Future-Bulk Heterojunction Polymer Solar Cells with Power Conversion Efficiency of 7.4%. *Adv. Mater.* **22,** E135–E138 (2010).
4. Service, R. F. Outlook Brightens for Plastic Solar Cells. *Science* **332,** 293–293 (2011).
5. Shirakawa, H., Louis, E. J., MacDiarmid, A. G., Chiang, C. K. & Heeger, A. J. Synthesis of electrically conducting organic polymers: halogen derivatives of polyacetylene, (CH) x. *J. Chem. Soc. Chem. Commun.* 578 (1977). doi:10.1039/c39770000578
6. Tang, C. W. Two-layer organic photovoltaic cell. *Appl. Phys. Lett.* **48,** 183 (1986).
7. Sariciftci, N. S., Smilowitz, L., Heeger, A. J. & Wudl, F. Photoinduced Electron Transfer from a Conducting Polymer to Buckminsterfullerene. *Science* **258,** 1474–1476 (1992).
8. Pettersson, L. A. A., Roman, L. S. & Inganäs, O. Modeling photocurrent action spectra of photovoltaic devices based on organic thin films. *J. Appl. Phys.* **86,** 487 (1999).
9. Yu, G., Gao, J., Hummelen, J. C., Wudl, F. & Heeger, A. J. Polymer Photovoltaic Cells: Enhanced Efficiencies via a Network of Internal Donor-Acceptor Heterojunctions. *Science* **270,** 1789–1791 (1995).
10. Huang, J. *et al.* Annealing effect of polymer bulk heterojunction solar cells based on polyfluorene and fullerene blend. *Org. Electron.* **10,** 27–33 (2009).
11. Li, G. *et al.* 'Solvent Annealing' Effect in Polymer Solar Cells Based on Poly(3-hexylthiophene) and Methanofullerenes. *Adv. Funct. Mater.* **17,** 1636–1644 (2007).
12. Moon, J. S. *et al.* Effect of Processing Additive on the Nanomorphology of a Bulk Heterojunction Material †. *Nano Lett.* **10,** 4005–4008 (2010).
13. Giridharagopal, R. & Ginger, D. S. Characterizing Morphology in Bulk Heterojunction Organic Photovoltaic Systems. *J. Phys. Chem. Lett.* **1,** 1160–1169 (2010).
14. Germack, D. S. *et al.* Substrate-dependent interface composition and charge transport in films for organic photovoltaics. *Appl. Phys. Lett.* **94,** 233303 (2009).
15. Tillack, A. F. *et al.* Surface Characterization of Polythiophene:Fullerene Blends on Different Electrodes Using Near Edge X-ray Absorption Fine Structure. *Acs Appl. Mater. Interfaces* **3,** 726–732 (2011).
16. White, M. S., Olson, D. C., Shaheen, S. E., Kopidakis, N. & Ginley, D. S. Inverted bulk-heterojunction organic photovoltaic device using a solution-derived ZnO underlayer. *Appl. Phys. Lett.* **89,** 143517 (2006).
17. Li, G., Chu, C.-W., Shrotriya, V., Huang, J. & Yang, Y. Efficient inverted polymer solar cells. *Appl. Phys. Lett.* **88,** 253503 (2006).
18. Jørgensen, M., Norrman, K. & Krebs, F. C. Stability/degradation of polymer solar cells. *Sol. Energy Mater. Sol. Cells* **92,** 686–714 (2008).
19. Sista, S., Hong, Z., Chen, L.-M. & Yang, Y. Tandem polymer photovoltaic cells—current status, challenges and future outlook. *Energy Environ. Sci.* **4,** 1606 (2011).
20. H. Ishii, K. Sugiyama, E. Ito, K. Seki. Energy level alignment and interfacial electronic structures at organic/metal and organic/organic interfaces. *Adv. Mater.* **11,** 605 (1999).

21. Wei, Q., Nishizawa, T., Tajima, K. & Hashimoto, K. Self-Organized Buffer Layers in Organic Solar Cells. *Adv. Mater.* **20,** 2211–2216 (2008).
22. Jung, J. W., Jo, J. W. & Jo, W. H. Enhanced Performance and Air Stability of Polymer Solar Cells by Formation of a Self-Assembled Buffer Layer from Fullerene-End-Capped Poly(ethylene glycol). *Adv. Mater.* **23,** 1782–1787 (2011).
23. Li, C.-Z. *et al.* Effective interfacial layer to enhance efficiency of polymer solar cells via solution-processed fullerene-surfactants. *J. Mater. Chem.* **22,** 8574 (2012).
24. Zhang, Y. *et al.* Indacenodithiophene and Quinoxaline-Based Conjugated Polymers for Highly Efficient Polymer Solar Cells. *Chem. Mater.* **23,** 2289–2291 (2011).
25. Garcia-Belmonte, G. *et al.* Charge carrier mobility and lifetime of organic bulk heterojunctions analyzed by impedance spectroscopy. *Org. Electron.* **9,** 847–851 (2008).
26. Boix, P. P., Wienk, M. M., Janssen, R. A. J. & Garcia-Belmonte, G. Open-Circuit Voltage Limitation in Low-Bandgap Diketopyrrolopyrrole-Based Polymer Solar Cells Processed from Different Solvents. *J. Phys. Chem. C* **115,** 15075–15080 (2011).
27. Boix, P. P. *et al.* Role of ZnO Electron-Selective Layers in Regular and Inverted Bulk Heterojunction Solar Cells. *J. Phys. Chem. Lett.* **2,** 407–411 (2011).
28. S. Braun, W. R. Salaneck, M. Fahlman. Energy-level alignment at organic/metal and organic/organic interfaces. *Adv. Mater.* **21,** 1450 (2009).
29. Bisquert, J. & Garcia-Belmonte, G. On Voltage, Photovoltage, and Photocurrent in Bulk Heterojunction Organic Solar Cells. *J. Phys. Chem. Lett.* **2,** 1950–1964 (2011).
30. Cowan, S. R., Roy, A. & Heeger, A. J. Recombination in polymer-fullerene bulk heterojunction solar cells. *Phys. Rev. B* **82,** (2010).
31. Garcia-Belmonte, G. & Bisquert, J. Open-circuit voltage limit caused by recombination through tail states in bulk heterojunction polymer-fullerene solar cells. *Appl. Phys. Lett.* **96,** 113301 (2010).
32. Leong, W. L., Cowan, S. R. & Heeger, A. J. Differential Resistance Analysis of Charge Carrier Losses in Organic Bulk Heterojunction Solar Cells: Observing the Transition from Bimolecular to Trap-Assisted Recombination and Quantifying the Order of Recombination. *Adv. Energy Mater.* **1,** 517–522 (2011).
33. Maurano, A. *et al.* Recombination Dynamics as a Key Determinant of Open Circuit Voltage in Organic Bulk Heterojunction Solar Cells: A Comparison of Four Different Donor Polymers. *Adv. Mater.* **22,** 4987–4992 (2010).
34. Shuttle, C. *et al.* Bimolecular recombination losses in polythiophene: Fullerene solar cells. *Phys. Rev. B* **78,** (2008).
35. Hawks, S. A. *et al.* Relating Recombination, Density of States, and Device Performance in an Efficient Polymer:Fullerene Organic Solar Cell Blend. *Adv. Energy Mater.* n/a–n/a (2013). doi:10.1002/aenm.201300194
36. *Impedance spectroscopy: theory, experiment, and applications*. (Wiley-Interscience, 2005).
37. Kalyanasundaram, K. *Dye-sensitized Solar Cells*. (CRC Press, 2010).
38. Armbruster, O., Lungenschmied, C. & Bauer, S. Dielectric response of doped organic semiconductor devices: P3HT:PCBM solar cells. *Phys. Rev. B* **84,** (2011).
39. Büttiker, M., Thomas, H. & Prêtre, A. Mesoscopic capacitors. *Phys. Lett.* **180,** 364–369 (1993).
40. Bisquert, J. Chemical capacitance of nanostructured semiconductors: its origin and significance for nanocomposite solar cells. *Phys. Chem. Chem. Phys.* **5,** 5360 (2003).

41. Bisquert, J. & Garcia-Belmonte, G. On Voltage, Photovoltage, and Photocurrent in Bulk Heterojunction Organic Solar Cells. *J. Phys. Chem. Lett.* **2,** 1950–1964 (2011).
42. Nayak, P. K., Garcia-Belmonte, G., Kahn, A., Bisquert, J. & Cahen, D. Photovoltaic efficiency limits and material disorder. *Energy Environ. Sci.* **5,** 6022 (2012).
43. Guerrero, A., Marchesi, L. F., Boix, P. P., Bisquert, J. & Garcia-Belmonte, G. Recombination in Organic Bulk Heterojunction Solar Cells: Small Dependence of Interfacial Charge Transfer Kinetics on Fullerene Affinity. *J. Phys. Chem. Lett.* **3,** 1386–1392 (2012).
44. Garcia-Belmonte, G. *et al.* Charge carrier mobility and lifetime of organic bulk heterojunctions analyzed by impedance spectroscopy. *Org. Electron.* **9,** 847–851 (2008).
45. Garcia-Belmonte, G. *et al.* Influence of the Intermediate Density-of-States Occupancy on Open-Circuit Voltage of Bulk Heterojunction Solar Cells with Different Fullerene Acceptors. *J. Phys. Chem. Lett.* **1,** 2566–2571 (2010).
46. Boix, P. P. *et al.* Role of ZnO Electron-Selective Layers in Regular and Inverted Bulk Heterojunction Solar Cells. *J. Phys. Chem. Lett.* **2,** 407–411 (2011).
47. Ripolles-Sanchis, T., Guerrero, A., Bisquert, J. & Garcia-Belmonte, G. Diffusion-Recombination Determines Collected Current and Voltage in Polymer:Fullerene Solar Cells. *J. Phys. Chem. C* **116,** 16925–16933 (2012).
48. Maurano, A. *et al.* Transient Optoelectronic Analysis of Charge Carrier Losses in a Selenophene/Fullerene Blend Solar Cell. *J. Phys. Chem. C* **115,** 5947–5957 (2011).
49. Shuttle, C. G. *et al.* Experimental determination of the rate law for charge carrier decay in a polythiophene: Fullerene solar cell. *Appl. Phys. Lett.* **92,** 093311 (2008).
50. Chang-Zhi Li *et al.* in preparation
51. He, Y., Chen, H.-Y., Hou, J. & Li, Y. Indene−C_{60} Bisadduct: A New Acceptor for High-Performance Polymer Solar Cells. *J. Am. Chem. Soc.* **132,** 1377–1382 (2010).